

Investigation of satellite vertical sensitivity on long-term retrieved lower tropospheric ozone trends

Richard J. Pope^{1,2}, Fiona M. O'Connor^{3,4}, Mohit Dalvi³, Brian J. Kerridge^{5,6}, Richard Siddans^{5,6}, Barry G. Latter^{5,6}, Brice Barret⁷, Eric Le Flochmoen⁷, Anne Boynard^{8,9}, Martyn P. Chipperfield^{1,2}, Wuhu Feng^{1,10}, Matilda A. Pimlott¹, Sandip S. Dhomse^{1,2}, Christian Retscher¹¹, Catherine Wespes¹² and Richard Rigby^{1,13}

1: School of Earth and Environment, University of Leeds, Leeds, United Kingdom

2: National Centre for Earth Observation, University of Leeds, Leeds, United Kingdom

3: Met Office Hadley Centre, Exeter, United Kingdom

4: Department of Mathematics & Statistics, Global Systems Institute, University of Exeter, United Kingdom

5: Remote Sensing Group, STFC Rutherford Appleton Laboratory, Chilton, United Kingdom

6: National Centre for Earth Observation, STFC Rutherford Appleton Laboratory, Chilton, United Kingdom

7: Laboratoire d'Aérodynamique/OMP, Université de Toulouse, Toulouse, France

8: LATMOS/IPSL, Sorbonne Université, UVSQ, CNRS, Paris, 75005, France

9: SPASCIA, Ramonville-Saint-Agne, 31520, France

10: National Centre for Atmospheric Science, University of Leeds, Leeds, United Kingdom

11: European Space Agency, ESRI, Frascati, Italy

12: Université libre de Bruxelles (ULB), Spectroscopy, Quantum Chemistry and Atmospheric Remote Sensing, Brussels, Belgium

13: Centre for Environmental Modelling and Computation, University of Leeds, Leeds, United Kingdom

In preparation for *Atmospheric Chemistry and Physics*

Correspondence to: Richard J. Pope (r.j.pope@leeds.ac.uk)

Key Points

- Satellite lower tropospheric column ozone (LTCO₃) records in the northern hemisphere show small trends with large uncertainty ranges between 2008 and 2017. Satellite lower tropospheric column ozone (LTCO₃) trends in the northern hemisphere show small scale trends with large uncertainty ranges between 2008 and 2017.
- Modelled LTCO₃ over that period is temporally stable and application of the satellite averaging kernels (AKs), accounting for the vertical sensitivity, to the model yields little impact on the simulated trends.

Abstract:

Ozone is a potent air pollutant in the lower troposphere and an important short-lived climate forcer (SLCF) in the upper troposphere. Studies investigating long-term trends in tropospheric column ozone (TCO₃) have shown large-scale spatiotemporal inconsistencies. Here, we investigate the long-term trends in lower tropospheric column ozone (LTCO₃, surface-450 hPa sub-column) by exploiting a synergy of satellite and ozonesonde datasets and an Earth System Model (UKESM) over North America, Europe and East Asia for the decade 2008-2017. Overall, we typically find small LTCO₃ linear trends with large uncertainty ranges from the Ozone Monitoring Instrument (OMI) and the Infrared Atmospheric Sounding Interferometer (IASI), while

Formatted: Font colour: Auto

40 model simulations indicate a stable L_{TCO₃} tendency. Trends in the satellite apriori datasets show negligible
41 trends indicating that any year-to-year changes in spatiotemporal sampling over of these satellite data sets
42 over the period concerned has not influenced derived trends in Trends in the satellite a-priori datasets show
43 negligible trends indicating year-to-year sampling is not an issue. The application of the satellite averaging
44 kernels (AKs) to the UKESM ozone profiles, accounting for the satellite vertical sensitivity and allowing for
45 like-for-like comparisons, has a limited impact on the modelled L_{TCO₃} tendency in most cases. While, in
46 relative terms, this is more substantial (e.g. in the order of 100%), the absolute magnitudes of the model
47 trends show negligible change. However, as the model has a near-zero tendency, artificial trends were
48 imposed on the model time-series (i.e. L_{TCO₃} values rearranged from smallest to largest) to test the
49 influence of the AKs but simulated L_{TCO₃} trends remained small. Therefore, the L_{TCO₃} tendency between
50 2008 and 2017 in northern hemispheric regions are likely small, with large uncertainties, and it is difficult to
51 detect any small underlying linear trends due to inter-annual variability or other factors which require
52 further investigation. (e.g. the radiative transfer scheme (RTS) used and/or the inputs (e.g. meteorological
53 fields) used in the RTS).

Formatted: Font colour: Auto

Formatted: Font colour: Auto

54

55 1. Introduction

56 Tropospheric ozone (TO₃) is a short-lived climate forcer (SLCF) and an important greenhouse gas (GHG;
57 Myhre et al., 2013; Forster et al., 2021). TO₃ is also a hazardous air pollutant with adverse impacts on human
58 health (Doherty et al., 2017; WHO, 2022) and agricultural/natural vegetation (Sitch et al., 2007; Hollaway et
59 al., 2012). Since the pre-industrial (PI) period, anthropogenic activities have increased the atmospheric
60 loading of ozone (O₃) precursor gases, most notably methane (CH₄) and nitrogen oxides (NO_x) resulting in an
61 increase in TO₃ of 25-50% since 1900 (Gauss et al., 2006; Lamarque et al., 2010; Young et al., 2013). The PI to
62 present day (PD) radiative forcing (RF) from TO₃ is estimated by the Intergovernmental Panel on Climate
63 Change (IPCC) to be 0.47 Wm⁻² (Forster et al., 2021) with an uncertainty range of 0.24-0.70 Wm⁻².

64 During the satellite-era (i.e. since the mid-1990s), extensive records of TO₃ have been produced, e.g. by the
65 European Space Agency Climate Change Initiative (ESA-CCI; ESA, 2019). However, the large ~~presents~~
66 presence of stratospheric O₃, coupled with the different vertical sensitivities and sources of error associated
67 with observations in different wavelength regions (e.g. Eskes and Boersma 2003; Ziemke et al., 2011; Miles
68 et al., 2015) means large-scale inconsistencies in time and space exist between the records of satellite
69 tropospheric column ozone (TCO₃) (as shown by Gaudel et al., 2018).

70 The work by Gaudel et al. (2018) was part of the Tropospheric Ozone Assessment Report (TOAR), which
71 represented a large global effort to understand spatio-temporal patterns and variability in TO₃. ~~However,~~
72 ~~†~~ their investigation of ozonesondes (2003-2012) and products from nadir viewing satellites in polar orbits
73 (three from the Ozone Monitoring Instrument (OMI) (2005-2015/6) and two from the Infrared Atmospheric
74 Sounding Interferometer (IASI) (2008-2016)) displayed discrepancies in the spatial distribution, magnitude,
75 direction and significance of the TCO₃ trends. They noted that the records cover slightly different time
76 periods but were unable to provide any definitive reasons for these discrepancies beyond briefly suggesting
77 that differences in measurement techniques and retrieval methods were likely to be causing the observed
78 spatial inconsistencies. The range of potential definitions of the tropopause height used to derive TCO₃ from
79 these nadir-viewing profile products could also lead to differences between the satellite product absolute
80 values and their temporal evolution. While the 5 products discussed above use the same definition (i.e.
81 World Meteorological Organisation (WMO) 2 K/km lapse rate; WMO, 1957), several of the other products
82 analysed by Gaudel et al. (2018) did use other definitions.

Formatted: Font colour: Auto

83 The vertical sensitivity of each retrieved product (function of measurement technique and retrieval
84 methodology) used by Gaudel et al. (2018) will have had an impact on which part of the troposphere the O₃
85 signal is weighted towards. This is potentially one of the drivers behind the different OMI and IASI TCO₃
86 trends, where OMI showed predominantly positive trends between 60°S and 60°N while the opposite was
87 the case for IASI. This was evident in the OMI and IASI TCO₃ trends, where OMI showed predominantly
88 positive trends between 60°S and 60°N while the opposite was the case for IASI. The vertical sensitivity is
89 represented by the “averaging kernel” (AK), which provides the relationship between perturbations at
90 different levels in the retrieved and true profiles (Eskes and Boersma, 2003). Typically, for the products used
91 by Gaudel et al., (2018), the peak AK sensitivities for TO₃ are in the 0-6 km range for OMI (Miles et al., 2015)
92 and around 11-12 km for IASI (Keim et al., 2009), while there is a secondary peak at approximately 5 km
93 (Boynard et al., 2009). In the case of the Rutherford Appleton Laboratory (RAL) Space OMI data, used in
94 Gaudel et al., (2018), TCO₃ values were derived from retrieved surface – 450hPa layer average mixing ratios
95 applied also to the overlying 450hPa – tropopause layer using ERA-Interim profiles. As the TO₃ values were
96 derived from different (UV and IR) sensors and methodologies whose vertical sensitivities differ, they were
97 likely representing O₃ controlled by different contributions of atmospheric processes (e.g. precursor
98 emissions from the surface and stratosphere-troposphere exchanges). Therefore, TCO₃ trends from the
99 different satellite products are not necessarily expected to be similar. The determination of the linear trend
100 in a satellite TCO₃ record(s) can also be difficult as many factors (e.g. chemistry, emissions, deposition and
101 transport) control ozone interannual variability, especially on time-periods of a decade or less (Barnes et al.,
102 2016; Change et al., 2020; Fiore et al., 2022).

Formatted: Font colour: Auto

103 In this study, we undertake the first assessment of spatio-temporal variability in satellite-derived lower
104 tropospheric column ozone (LTCO₃, surface-450 hPa) from three instruments over a consistent decade
105 (2008-2017). In combination with an Earth System Model (ESM), we aim to quantify the impact of year-to-
106 year spatiotemporal sampling ~~year-to-year sampling~~, the satellite instrument uncertainties and the
107 instrument vertical sensitivity on long-term LTCO₃ trends. We focus our analysis on North America, Europe
108 and East Asia given their large emissions of ozone precursor gases and temporal variability. In our
109 manuscript, **Section 2** discusses the satellite/ozonesonde datasets and model used, **Section 3** presents our
110 results, and our discussion/ conclusions are summarised in **Sections 4 and 5**.

Formatted: Font colour: Auto

Formatted: Font colour: Auto

111 2. Methodology and Datasets

112 2.1. Satellite Datasets

113 The satellite products (see **Table 1**) used here are from nadir-viewing polar-orbiting platforms providing
114 ozone sub-column profiles. This includes ozone profile data from the OMI product developed by the RAL
115 Space and the IASI products from the Laboratoire d'aérodologie (IASI-SOFRID) and the Université Libre de
116 Bruxelles, in collaboration with the Laboratoire Atmosphères, Observations Spatiales (ULB-LATMOS) (IASI-
117 FORLI). OMI and IASI are on NASA's Aura and Eumetsat's MetOp-A satellites in sun-synchronous low Earth
118 orbits with local overpass times of 13.30 and 9.30, respectively. OMI and IASI are ultraviolet-visible (UV-Vis)
119 and infrared (IR) sounders with spectral ranges of 270-500 nm (Boersma et al., 2008, Boersma et al., 2011)
120 and 645-2760 cm⁻¹ (Illingworth et al., 2011), respectively. OMI has a spatial footprint at nadir of 24 km × 13
121 km, while IASI measures simultaneously in four fields of view (FOV, each circular at nadir with a diameter of
122 12 km) in a 50 km × 50 km square which are scanned across track to sample a 2200 km-wide swath (Clerbaux
123 et al., 2009).

124 The OMI retrieval scheme is based on an optimal estimation (OE) approach, produced by RAL Space, which is
125 described in detail by Miles et al., (2015). The retrieval schemes for IASI-FORLI and IASI-SOFRID O₃ are
126 discussed in detail by Boynard et al., (2018) and Barret et al., (2020). The lowest sub-column in the OMI sub-
127 column profile represents the surface-450 hPa layer (i.e. LTCO₃). For the IASI products, there were several

Formatted: Font colour: Auto

128 sub-columns spanning the surface to 450 hPa range. Therefore, the IASI sub-columns were totalled up
129 between the surface and the layer beneath or equal to the 450 hPa level. Where the 450 hPa level was
130 located within a sub-column (i.e. was located between its bounding upper and lower pressure levels), the
131 sub-column proportion between the lower pressure barrier and the 450 hPa level was determined and
132 added to the sub-columns below (i.e. towards the surface). For the ozone a priori profile, the RAL Space and
133 FORLI schemes use the ozone latitude vs month of year climatology of McPeters et al. (2007), while IASI-
134 SOFRID uses the dynamical ozone climatology described in Sofieva et al. (2014). However, the FORLI scheme
135 uses a single ozone profile (Boynard et al., 2018) derived from the McPeters et al. (2007) dataset, so has no
136 seasonality nor latitude dependence unlike the other retrieval schemes.

Formatted: Font colour: Auto

137 In this work, the OMI data were filtered for good quality retrievals where the geometric cloud fraction was
138 <0.2, the sub-column O₃ values were > 0.0, the solar zenith angle < 80.0°, the retrieval convergence flag = 1.0
139 and the normalised cost function was < 2.0. The IASI-FORLI data were filtered for a geometric cloud fraction
140 <0.13 (pre-filtered), degrees of freedom > 2.0, O₃ values > 0.0, solar zenith angle < 80.0° and the surface to
141 450 hPa sub-column O₃ / total column O₃ < 0.085. The IASI-SOFRID data were provided on a 1.0°×1.0°
142 horizontal grid (i.e. level 3 product, but at a daily temporal resolution – we use the daytime data in this
143 study) with filtering already applied in Barret et al., (2020). Here, only O₃ values > 0.0 were used. To remove
144 systematic biases between the satellite records, while maintaining the long-term inter-annual variability of
145 each record, ozonesondes were used to generate bias correction offsets (BCOs) (2008-2017) to help
146 harmonise the data sets (i.e. subtraction term in units of Dobson units, DU - as done in Russo et al. (2023)
147 and Pope et al. (2024)) and is discussed in the Supplementary Material (SM) (i.e. S1) To remove systematic
148 biases between the satellite records, ozonesondes were used to generate bias correction factors (2008-
149 2017) to help harmonise the data sets.

Formatted: Font colour: Auto

Formatted: Font colour: Auto

Formatted: Font colour: Auto

150 Here, each ozonesonde profile was co-located with the nearest satellite retrieval within 500 km and 6 hours
151 to reduce spatiotemporal sampling biases (e.g. Keppens et al., 2019). The ozonesonde sonde profile was
152 then interpolated in the vertical onto the satellite pressure grid where the sub-columns between pressure
153 levels were determined. The ozonesonde sub-column profiles were then convolved by the satellite averaging
154 kernels (AKs), which represent the satellite's sensitivity to retrieval ozone as a function of altitude. Thus,
155 allowing for a robust like-for-like comparison between the ozonesondes and the retrieved LTCO₃. The
156 application of AKs to ozonesonde profiles to evaluate satellite ozone products is discussed in detail by Pope
157 et al. (2023). The application of the AKs to the ozonesondes (and the model) is outlined in Equation 1:

Formatted: Font colour: Auto

$$158 \quad \text{sonde}_{AK} = AK(\text{sonde}_{int} - apr) + apr \quad (1)$$

Formatted: Font colour: Auto

159 where sonde_{AK} is the modified ozonesonde sub-column profile (Dobson units, DU), AK is the averaging kernel
160 matrix, sonde_{int} is the sonde sub-column profile (DU) on the satellite pressure grid and apr is the a priori
161 (DU). The application of the AKs to the ozonesondes is discussed in more detail in the SM S1. This is discussed
162 in the Supplementary Material (i.e. S1). The application of the satellite AKs to the ozonesondes and the
163 model is also discussed in S1.

Formatted: Font colour: Auto

Formatted: Font colour: Auto

Formatted: Font colour: Auto

Formatted: Font colour: Auto

164 To investigate long-term trends over North America, Europe and East Asia, the Hemispheric Transport of Air
165 Pollution (HTAP) regional sea-land mask (European Commission (2016); see S2, Figure S2), is used to sub-
166 sample the gridded satellite data for the respective regions and then generate average monthly time-series
167 for each product over each region of interest. To investigate long-term trends over North America, Europe
168 and East Asia, the Hemispheric Transport of Air Pollution (HTAP) regional sea-land mask (European
169 Commission (2016); see S2, Figure S2), is used to generate average monthly time series for each product
170 over each region of interest. For the ozonesonde time-series for each HTAP region investigated, only
171 ozonesonde sites which are located within each HTAP region are selected. This results in 15, 13 and 6
172 ozonesonde sites for North America, Europe and East Asia, respectively. As ozonesonde data for East Asia
173 are all from Japan, Taiwan and Hong Kong, trends in ozone LTCO₃ will likely be different to satellite/model
174 trends over all East Asia.

Formatted: Font: Bold

Formatted: Font: Bold

Formatted: Font colour: Auto

175 In Section 3.2, where we discuss the impact of satellite retrieval errors on derived LTCO₃ linear trends, the
176 OMI and IASI-FORLI retrieval errors are provided in their product files, but are not available for IASI-SOFRID.
177 Therefore, while not a perfect metric to represent the error in the IASI-SOFRID data, we use the standard
178 deviation in the monthly-spatial average of the regional time-series.

179 2.2. United Kingdom Earth System Model (UKESM)

180 The UK's Earth System Model, UKESM1.0, is a state-of-the-art ESM with fully interactive coupled component
181 models (e.g. atmosphere, ocean, land surface, atmospheric chemistry), which has been developed by the UK
182 Met Office and the Natural Environment Research Council (NERC). The detailed coupling of all the Earth
183 System components is described by Sellar et al. (2019). However, in this study, we run UKESM1.0 in an
184 atmosphere only configuration (e.g. similar to Archibald et al., (2020)). The aim is to use UKESM1.0 to
185 investigate long-term trends in TO₃ and help explore inconsistencies between satellite records, so it is
186 computationally more time efficient as only the atmospheric dynamics and chemistry components are
187 simulated. Over the 2008-2017 time period (with a 1-year spin up), the UKESM1.0 model tracers and
188 diagnostics (e.g. ozone, pressure) are output as 3D fields at sub-daily (6-hourly) time steps to allow robust
189 comparisons between the model and satellite data sets (i.e. model-satellite spatio-temporal co-location to
190 reduce representation biases and application of the satellite AKs to map the instrument vertical sensitivity
191 onto the model yielding like-for-like comparisons). The satellite AKs from OMI and IASI-FORLI are provided in
192 the level-2 files (i.e. an AK matrix per retrieval). However, the IASI-SOFRID AKs are provided from the gridded
193 level-3 data product (i.e. an AK matrix for each 1°×1° grid box).

194 Here, the UKESM1.0 land and atmosphere share a regular latitude–longitude grid with a resolution of 1.25°
195 ×1.875° with 85 vertical levels on a terrain-following hybrid height coordinate with a model lid at 85 km
196 above sea level (50 levels are below 18 km). All the key inputs to the model from other Earth system
197 components (e.g. sea surface temperature (SST) and land surface vegetation) were prescribed from ancillary
198 files. The ocean and ice forcing are represented by the monthly Reynolds sea ice and SSTs data from the
199 National Oceanic and Atmospheric Administration (NOAA, [https://climatedataguide.ucar.edu/climate-](https://climatedataguide.ucar.edu/climate-data/)
200 [data/](https://climatedataguide.ucar.edu/climate-data/)). Solar forcings are provided by Phase 6 of the Coupled Model Intercomparison Project (CMIP6;
201 Matthes et al., 2017; Eyring et al., 2016), as is the stratospheric aerosol climatology to represent
202 contributions from volcanic eruptions (Sellar et al., 2019). The land cover is provided from output from the
203 land surface component of the ESM (JULES; Wiltshire et al., 2021) from a fully coupled historical simulation.
204 Anthropogenic and biomass burning emissions from Hoesly et al. (2018) and van Marle et al. (2017) are
205 prescribed for the period 2008 to 2014. After 2014, anthropogenic and biomass burning emissions are from
206 the Shared Socioeconomic Pathway (SSP, Rao et al., 2017) 2-4.5 (i.e. a middle-of-the-road climate and
207 emissions scenario).

208 Biological emissions are a climatology between 2001 and 2010 from the MEGAN-MACC data base
209 (Sindelarova et al., 2014), while natural emissions are from the Precursors of Ozone and their Effects in the
210 Troposphere (POET, http://accent.aero.jussieu.fr/database_table_inventories.php) based on 1990. Dry
211 deposition of O₃ to the land surface is represented by the Wesley scheme, which is applied as in O'Connor et
212 al., (2014). The model is also in a nudged or “specified dynamics” configuration (i.e. meteorological analyses
213 are used to “nudge” the model's meteorological variables, i.e. u- and v-wind components, and potential
214 temperature, towards reality; Telford et al., 2008) using 6-hourly reanalysis data from the European Centre
215 for Medium-Range Weather Forecasts (ECMWF) ERA-Interim product. A similar configuration of UKESM1.0
216 was used by Archibald et al., (2020), in which a thorough evaluation against multiple observations (e.g.
217 surface, aircraft and satellite) was carried out.

Formatted: Font colour: Auto

2.3. Trend Approach

LTCO₃ trends are calculated using the linear least squares fit approach of van der A et al., (2006; 2008), and utilised by Pope et al., (2018) who investigated LTCO₃ trends. Here, the monthly LTCO₃ time-series are represented by the function:

$$Y_t = C + BX_t + A\sin(\omega X_t + \phi) + N_t \quad (12)$$

where Y_t is the observed monthly LTCO₃ for month t , X_t is the number of months since the start of the record, C is the first monthly mean LTCO₃ value of the record, B is the monthly linear trend and $A\sin(\omega X_t + \phi)$ is the seasonal model component (Weatherhead et al., 1998). A is the amplitude, ω is the frequency (set to 1 year; $\omega=\pi/6$) and ϕ is the phase shift. C , B , A and ϕ are the fit parameters from the linear least squares fit. N_t represents the model errors/residuals. The linear trend uncertainty, σ_B , represents the trend precision and is calculated as:

$$\sigma_B = \left[\frac{\sigma_N}{n^2} \frac{(1+\alpha)}{(1-\alpha)} \right] \quad (23)$$

where n is the number of years, α is the autocorrelation in the residuals (N_t) and σ_N is the standard deviation in the residuals. As in van der A et al., (2006) and Pope et al., (2018), we calculate the autocorrelation for each time-series using a lag of one-time step (i.e. one month). The autocorrelation in Equation 12 is not accounted for directly, so is factored into the trend uncertainty (Equation 23), as used and discussed by van der A et al., (2006) and Weatherhead et al., (1998), respectively.

3. Results

A detailed evaluation of UKESM1.0 LTCO₃ through comparisons with the three satellite products and ozonesondes is presented in S3. Overall, UKESM1.0 robustly simulates LTCO₃ spatially and seasonally in comparison to the ozonesondes and satellite instruments (i.e. typically within the ozonesonde variability and satellite uncertainty range).

3.1. UKESM1.0 and Satellite LTCO₃ Trends

3.1.1. North America

LTCO₃ trends from OMI, IASI-FORLI, IASI-SOFRID and ozonesondes are derived between 2008 and 2017 (i.e. consistent time record for all instruments) using the linear-seasonal trend model (Equation 12). For each satellite product, the corresponding UKESM1.0 time-series (with and without AKs) are analysed as well as the satellite apriori. For the North America OMI metrics (Figure 1 – top left, Table 2), there is clear seasonality in the apriori ranging between approximately 17.0 and 22.0 Dobson Units (DU). As this is based on the climatology of McPeters et al., (2007), there is no trend and there is a very good model fit (i.e. $R^2=1.0$). The key point is that, as a climatology, the apriori will have no trend but if there are substantial temporal sampling differences between years, then an artificial trend could be introduced. OMI LTCO₃ ranges between 20.0 and 27.0 DU with substantial variability. There is a drop in LTCO₃ to 19.0 DU in 2009 before peaking at 25.0-27.0 DU between 2010 and 2015. Peak LTCO₃ then drops to 22.0-24.0 DU in 2016 and 2017. As a result, the linear-seasonal trend model, which does not account for interannual variations such as this, only has a fit skill of $R^2=0.59$. The corresponding OMI LTCO₃ trend is -0.79 (-7.07, 5.48; 95% confidence interval, $-p$ value = 0.89) DU/decade showing a negligible trend with a large uncertainty range. Here, -0.79 DU/decade is the trend while the -7.07 and 5.48 DU/decade values are the 95% confidence interval. The UKESM1.0 LTCO₃ time-series ranges between 17.0 and 22.0 DU with clear seasonality, though somewhat less inter-annual variation than OMI, and the linear-seasonal trend model therefore has a considerably better fit with $R^2=0.95$. The model trend has the opposite sign at 0.21 (-0.37, 0.78; $-p=0.59$) DU/decade. Here, the

Formatted: Font: Italic

Formatted: Font: Bold

Formatted: List Paragraph, Outline numbered + Level: 3 + Numbering Style: 1, 2, 3, ... + Start at: 1 + Alignment: Left + Aligned at: 0.63 cm + Indent at: 1.9 cm

259 model trend is near-zero with a relatively large uncertainty range (though not as sizable as OMI). When the
260 AKs are applied to the model, the trend switches sign to -0.57 (-1.58, 0.45; $p=0.98$) DU/decade and the
261 linear-seasonal trend model fit decreases in skill to $R^2=0.90$. The trend switch of sign, though small, is
262 potentially linked to the application of the AKs, which also increases LTCO₃ by 2.0-3.0 DU in general.

263 We also investigated the satellite degrees of freedom of signal (DOFS) over the lower troposphere (i.e.
264 surface to 450 hPa), which provides an estimate of the number of independent pieces of information in the
265 LTCO₃. The DOFS are calculated by taking the trace of the AK matrix over the lower tropospheric levels in the
266 satellite vertical grid. Overall, we found that the products for the three regions had negligible trends in their
267 time-series (i.e. within ± 1.0 %/year) meaning that the information content of satellite LTCO₃ had remained
268 stable with time (see S3).

269 The IASI-FORLI LTCO₃ time-series (**Figure 1 – top right**) tends to be lower than OMI and range between 17.0
270 and 22.0 DU. There is a substantial negative IASI-FORLI trend (-1.42 (-2.35, -0.50; $p=0.00$) DU/decade);
271 **Table 2)** though as stated by Boynard et al., (2018) and Wespes et al., (2018) though as suggested by Boynard
272 et al., (2018) and Wespes et al., (2018), the input IASI Level-1 data sets into the FORLI retrieval are not
273 consistent with time; they suffer from a specific discontinuity in September 2010 which degrades the
274 robustness of this trend. While we are aware of the artificial trend in the IASI-FORLI dataset, it is still a
275 valuable long-term product allowing us to quantify multiple factors (e.g. impact of AKs on model
276 tendencies/absolute values and year-to-year spatiotemporal sampling year-to-year sampling stability – i.e.
277 near-zero trend in the apriori). The apriori has a negligible trend but there is no clear seasonality in the
278 apriori time-series. As a result, the linear-seasonal trend model has a more limited fit skill (i.e. $R^2=0.67$). The
279 impact of the satellite AKs appears to have less impact for IASI-FORLI as both UKESM1.0 and UKESM1.0+AKs
280 have time-series ranging between approximately 17.0 and 21.0 (though slightly smaller UKESM1.0+AKs
281 range) and linear-seasonal trend model fits of $R^2=0.93$ and $R^2=0.92$, respectively. The corresponding trends
282 are small at -0.13 (-0.75, 0.49; $p=0.67$) and -0.32 (-0.82, 0.20; $p=0.22$) DU/decade, but the introduction of
283 the AKs does move the UKESM1.0 trend slightly towards that of the satellite. Interestingly, while the
284 application of the IASI-FORLI AKs to UKESM marginally pushes the convolved model trend in LTCO₃ towards
285 that of the satellite (which has a substantial negative trend), the IASI-FORLI DOFS actually have small positive
286 trends (0.37-0.57 %/year – see S3). Therefore, there is minor scale, yet contrasting, discrepancy in how the
287 vertical sensitivity is influencing the long-term LTCO₃ trends.

288 For IASI-SOFRID (**Figure 1 – bottom left**), there is little difference between any of the time-series as they all
289 range between 16.0 and 21.0 DU with corresponding linear-seasonal trend model fits of $R^2=0.94$ to 0.98 and
290 negligible trends. The IASI-SOFRID and apriori trends are 0.12 (-0.59, 0.82; $p=0.74$) and 0.11 (-0.17, 0.39; $p=$
291 0.43) DU/decade; **Table 2)**, respectively, with the model showing near-zero trends in both cases. Given the
292 close agreement between the satellite and apriori time series and fit metrics, it is suggestive that IASI-
293 SOFRID TO₃ is more closely confined to the apriori profile than are the other products. The ozonesondes
294 show a substantial trend of -1.15 (-2.0, -0.10; $p=0.03$) DU/decade, while the model trend sampled as the
295 sondes is -0.16 (-1.67, 1.35; $p=0.63$) DU/decade. The co-located model and ozonesonde linear-seasonal
296 trend model fits are $R^2=0.62$ and 0.64, respectively. The noise and lack of seasonality in the ozonesonde
297 time-series is slightly unexpected given the reasonable density of stations over North America, though the
298 spatial coverage and temporal sampling is much less than the satellite products.

299 3.1.2. Europe

300

Formatted: Font colour: Auto

Formatted: Font: Not Bold

Formatted: Font colour: Auto

Formatted: Font colour: Auto

Formatted: Font colour: Auto

Formatted: Outline numbered + Level: 3 + Numbering Style: 1, 2, 3, ... + Start at: 1 + Alignment: Left + Aligned at: 0.63 cm + Indent at: 1.9 cm

301 In Europe, the OMI LTCO₃ values are larger than in North America, ranging between 19.0 and 30.0 DU (**Figure**
302 **2 – top left**). The same inter-annual variability exists, peaking between 2010 and 2015 with the minimum in
303 2009. Hence, the linear-seasonal trend model, which does not represent interannual variation, does not
304 have high skill and R²=0.72. The corresponding trend is -0.80 (-7.29, 5.69; **p=0.89**) DU/decade, so has a
305 similar direction and magnitude to that for North America, though is not substantial. The apriori ranges
306 between 17.0 and 22.5 DU with a trend of -0.12 (-0.26, 0.03; **p=0.10**; **Table 2**) DU/decade. Given the
307 relatively small trend and uncertainty range, unlike the OMI equivalent, it suggests there is unlikely to be an
308 artificial trend arising through year-to-year spatiotemporal sampling year-to-year changes in geographical
309 sampling across the European region. UKESM1.0 LTCO₃ ranges between approximately 19.0 and 22.0 DU
310 with a good linear-seasonal trend model fit of R²=0.99 and a trend of -0.11 (-0.50, 0.29; **p=0.59**) DU/decade.
311 As for North America, when the OMI AKs are applied, the UKESM LTCO₃ values systematically increase by
312 2.0-3.0 DU, move further away from the satellite apriori and more closely follow the variability of OMI
313 (although R² decreases slightly to 0.95). The trend tends towards that of OMI at -0.72 (-1.77, 0.32; **p=0.16**)
314 DU/decade. As in the case of North America, the European IASI-FORLI apriori has no seasonal cycle (and
315 moderate R² of 0.48 in the linear-seasonal trend model fit) with a near-zero trend (0.09 (-0.09, 0.27; **p=0.32**)
316 DU/decade) (**Figure 2 – top right, Table 2**).

Formatted: Font colour: Auto

317 The IASI-FORLI data exhibit a substantial negative trend of -1.83 (-2.78, 0.89; **p=0.00**) DU/decade, again due
318 to again potentially attributable to step changes in the IASI Level-1 processor, with a good linear-seasonal
319 trend model fit of R²=0.92. UKESM1.0 LTCO₃ trends, without and with AKs applied, are -0.28 (-0.77, 0.20; **p=**
320 **0.25**) and -0.43 (-1.21, 0.35; **p=0.27**) DU/decade. Again, though a small change, the application of the AKs
321 introduces a slight perturbation of the model trend compared to IASI-FORLI. The IASI-SOFRID apriori, ranging
322 between 17.0 and 21.0 DU, has a trend of 0.17 (-0.12, 0.45; **p=0.24**) DU/decade with good fit skill of R²=0.98
323 (**Figure 2 – bottom left**).

Formatted: Font colour: Auto

324 The IASI-SOFRID and UKESM1.0 metrics, with and without averaging kernels applied, are similar, with LTCO₃
325 trends of 0.05 (-0.91, 1.01; **p=0.92**), -0.27 (-0.72, 0.19; **p=0.24**) and 0.08 (-0.33, 0.49; **p=0.69**) DU/decade,
326 respectively, and with R² values between 0.93 and 0.98. The ozonesonde monthly regional means (**Figure 2 –**
327 **bottom right**) has a more pronounced time-series than North America, yielding a less noisy time-series of
328 LTCO₃. Here, there is clear seasonality ranging between 17.0 and 24.0 DU with a large R² value of 0.95. The
329 ozonesonde trend is relatively small at -0.61 (-1.39, 0.17; **p=0.12**) DU/decade while the UKESM1.0
330 equivalent is more substantial at -0.96 (-1.56, 0.35; **p=0.00**) DU/decade.

3.1.3. East Asia

Formatted: Outline numbered + Level: 3 + Numbering Style: 1, 2, 3, ... + Start at: 1 + Alignment: Left + Aligned at: 0.63 cm + Indent at: 1.9 cm

332 For East Asia, OMI LTCO₃ again has both a pronounced seasonal cycle and inter-annual variability (19.0-27.0
333 DU), consistent with the other two regions discussed above (**Figure 3 – top left**). This yields a moderate skill
334 fit to the linear-seasonal trend model of R²=0.52 and near-zero trend (-0.09 (-7.88, 7.70; **p=0.98**)
335 DU/decade). The apriori has a trend of -0.25 (-0.71, 0.22; **p=0.29**) DU/decade, so year-to-year
336 spatiotemporal sampling year-to-year sampling changes could be influencing the robustness of OMI
337 retrieved time-series in this region. However, both the instrument and apriori trend uncertainties intersect
338 with 0.0. UKESM1.0 LTCO₃ ranges between approximately 16.0 and 22.0 DU with a good fit R² of 0.98. Like
339 the other regions, the application of the OMI AKs increases the model values systematically by several DUs.
340 The UKESM1.0 LTCO₃ trend is -0.16 (-0.94, 0.62; **p=0.67**) DU/decade, which is small, but the AKs increase
341 the trend magnitude to -0.62 (-2.24, 1.00; **p=0.44**) DU/decade, which moves it away from the OMI trend.

Formatted: Font colour: Auto

342 IASI-FORLI (**Figure 3 – top right, Table 2**), like the other two regions, has a substantial negative trend of -1.52
343 (-2.16, 0.88; **p=0.00**) DU/decade. The apriori again exhibits virtually no seasonal cycle (low fit skill of

344 ~~R²=0.21) but non-zero and negligible year-to-year spatiotemporal sampling differences yielding a year-to-~~
 345 ~~year variation so a low fit skill of R²=0.21 and shows a~~ near-zero trend of -0.03 (-0.22, 0.16; p = 0.76)
 346 DU/decade. For UKESM1.0, the East Asian seasonal range is much larger than other regions, ranging
 347 between 17.0 and 27.0 DU (i.e. seasonal amplitude of approximately ±5.0 DU). When the AKs are applied,
 348 this range shrinks to approximately 19.0 to 23.0 DU, more in-line with the IASI-FORLI LTCO₃ values. The
 349 corresponding model trends are -0.03 (-0.62, 0.56; ~~p=0.93~~) DU/decade and -0.29 (-0.80, 0.22; ~~p=0.25~~)
 350 DU/decade, so the AKs are pushing the model tendency towards that of the instrument, though the impact
 351 is small in absolute terms (large in relative terms).

352 IASI-SOFRID and its apriori LTCO₃ seasonality are again very similar, ranging between 16.0 and 21.0 DU with
 353 very little interannual variability and with linear seasonal trend model fit skills of R²=0.96 and 0.98 (**Figure 3 –**
 354 **bottom left, Table 2**). The IASI-SOFRID and apriori linear trends are therefore also consistent at -0.19 (-1.01,
 355 0.63; ~~p=0.65~~) and -0.15 (-0.73, 0.58; ~~p=0.82~~) DU/decade. The UKESM1.0 seasonal variability is again large,
 356 between 17.0 and 26.0 DU, and, as in the case of IASI-FORLI, when the instrument AKs are applied to the
 357 model, the seasonal range shrinks (i.e. 16.0-22.0 DU) to be much closer to those of the retrieval and its prior.
 358 The model trends are -0.42 (-0.97, 0.13; ~~p=0.12~~) and -0.24 (-0.67, 0.20; ~~p=0.28~~) (with AKs) DU/decade,
 359 where there is a minor shift in the model tendency towards that of IASI-SOFRID and its prior. For the
 360 ozonesondes (**Figure 3 – bottom right**), there is a substantial LTCO₃ trend of 3.17 (0.16, 6.17; p = 0.04)
 361 DU/decade with a fit skill of R²=0.79, which is larger than those for North America and Europe. LTCO₃
 362 increases from 18.0-25.0 in 2008 to 21.0-28.0 in 2011. This remains similar in 2012 and 2013 before
 363 dropping by several DUs between 2014 and 2017. The UKESM1.0 sampled as the ozonesondes has
 364 considerably less inter-annual variability with a smaller trend of 0.37 (-0.90, 1.64; ~~p=0.56~~) DU/decade.
 365 Therefore, UKESM1.0 and the satellite product trends are generally smaller (in magnitude) than the
 366 ozonesonde tendencies. However, it is worth considering that there are only a few sites (e.g. Hong Kong and
 367 Taiwan) where ozonesonde data is available in East Asia.

368 **4.1.3.2. Influence of Satellite Averaging Kernels on UKESM1.0 LTCO₃**

369 To investigate the impact of applying the satellite averaging kernels to UKESM1.0, and thus learn something
 370 about vertical sensitivity influence on retrieved LTCO₃, three different metrics are considered for the 2008 to
 371 2017 time-period. These are the absolute LTCO₃ value, amplitude of the LTCO₃ seasonal cycle and the linear
 372 trend. These metrics are compared for the satellite, the satellite ± error term, the apriori, UKESM1.0 and
 373 UKESM1.0+AKs for the three regions discussed above.

374 From **Figure 4**, average OMI LTCO₃ is approximately 22.0, 24.0 and 23.0 DU for North America, Europe and
 375 East Asia, respectively. This represents a substantial deviation away from the apriori values of 17.5, 20.0 and
 376 16.0 DU, respectively. However, the average error term for OMI LTCO₃ is sizeable at approximately ±8.0 to
 377 ±9.0 DU for all regions. The average UKESM1.0 value for each region is approximately 19.5, 21.5 and 19.0 DU
 378 but the application of the AKs increases this by several DU to 22.0, 24.0 and 21.0 DU. In comparison, mean
 379 values for both IASI products vary less between the three geographical areas: IASI-FORLI (IASI-SOFRID) LTCO₃
 380 values are 20.0 (18.5), 19.0 (18.5) and 22.0 (18.0) DU, respectively. The corresponding error ranges, in
 381 comparison with OMI, are smaller between 17.0 and 23.0 (16.0 and 21.5), 16.0 and 21.5 (16.0 and 21.0) and
 382 18.0 and 23.5 (14.5 and 21.5) DU for North America, Europe and East Asia, respectively. With the IASI-FORLI
 383 AKs applied to UKESM1.0, LTCO₃ decreases from 19.5 to 19.25 DU, 21.25 to 19.5 DU and 22.75 to 21.25 DU
 384 for the three regions. For IASI-SOFRID, there is a decrease from 21.0 to 19.5 DU in Europe and a decrease
 385 from 22.0 to 19.5 DU in East Asia, while no change occurs in North America. Overall, OMI has the largest
 386 error range and the application of the AKs to UKESM1.0 systematically increases the model LTCO₃ time-

Formatted: Indent: Left: 0.63 cm, Hanging: 0.63 cm,
 Outline numbered + Level: 2 + Numbering Style: 1, 2, 3,
 ... + Start at: 1 + Alignment: Left + Aligned at: 0 cm +
 Indent at: 0.63 cm

387 series by several DU. The opposite occurs for the IASI products where there is a smaller decrease to
388 UKESM1.0 LTCO₃ of 1.0-2.0 DU. The error ranges are also smaller than that of OMI.

389 In terms of the LTCO₃ seasonal amplitude (**Figure 5**), OMI (including the error terms) is approximately 2.6
390 (for all) DU, 3.3-3.8 DU and 2.3-2.6 DU for North America, Europe and East Asia. The apriori seasonal
391 amplitude ranges from 2.7 to 2.9 DU across the regions. The IASI-FORLI averages (including the error terms)
392 tend to be lower than OMI but have similar seasonal ranges. North America, Europe and East Asia have
393 amplitudes of 2.3-2.5 DU, 2.3-2.5 DU and 1.6-1.8 DU, respectively. It is noteworthy that this seasonal cycle is
394 despite the IASI-FORLI prior exhibiting virtually no seasonal cycle at all. IASI-SOFRID has a European range of
395 2.4-2.6 DU, and comparable ranges for North America and East Asia at 1.8-2.5 DU and 2.3-3.0 DU. Therefore,
396 seasonal amplitude in IASI-SOFRID is more sensitive to the error metric but as the “error” term is based on
397 the LTCO₃ standard deviation, given the lack of an error term in the product, it is unsurprising that there is
398 more variability in the seasonal amplitude. For the OMI comparisons, the application of the AKs to
399 UKESM1.0 shifts the simulated amplitude slightly upwards from 2.0 to 2.1 DU, 3.1 to 3.3 DU and 4.0 to 4.4
400 DU for the respective regions. The IASI-FORLI AK impacts are a decrease from 1.9 to 1.4 DU, 3.0 to 2.1 DU
401 and 4.2 to 1.9. For IASI-SOFRID, the corresponding impact on UKESM1.0 is 2.2 to 2.4 DU, 3.3 to 2.9 and 4.5 to
402 3.2 DU. Therefore, the OMI AKs have a minimal impact, increasing the model seasonal amplitude by 0.1-0.3
403 DU, but the IASI products suppress the simulated amplitude by 1.0-2.0 DU at the most extreme.

404 The impact of the satellite LTCO₃ error terms on the derived linear trends are shown in **Figure 6**. For OMI,
405 the range in trends calculated (i.e. satellite ± error term) is approximately -1.50 (-7.04, 4.04; *p*=0.59) to -
406 0.09 (-6.98, 6.81; *p*=0.98) DU/decade, -1.65 (-6.92, 3.62; *p*=0.53) to 0.05 (-7.44, 7.53; *p*=0.99) DU/decade
407 and -1.05 (-6.61, 4.52; *p*=0.70) to 0.87 (-8.24, 9.98; *p*=0.85) DU/decade for North America, Europe and East
408 Asian, respectively. The IASI-FORLI trends (i.e. satellite ± error term) are substantial, ranging from -1.50 (-
409 2.51, -0.50; *p*=0.00) to -1.34 (-2.21, -0.47; *p*=0.00) DU/decade, -1.87 (-2.87, -0.87; *p*=0.00) to -1.80 (-2.72, -
410 0.88; *p*=0.00) DU/decade and -1.62 (-2.27, -0.98; *p*=0.00) to -1.42 (-2.06, -0.78; *p*=0.00) for the three
411 regions, respectively. The corresponding IASI-SOFRID trends were 0.09 (-0.48, 0.66; *p*=0.75) to 0.14 (-0.59,
412 0.88; *p*=0.70) DU/decade, -0.07 (-0.91, 0.78; *p*=0.87) to 0.16 (-0.74, 1.07; *p*=0.72) DU/decade and -0.30 (-
413 1.02, 0.42; *p*=0.41) to -0.08 (-0.73, 0.58; *p*=0.82), respectively. Therefore, only the IASI-FORLI trends (i.e.
414 satellite ± error term) are substantially different from zero (i.e. *p* < 0.05). However, that is likely due in part
415 to discontinuities in the Level-2 input meteorological data used to generate this version of the product
416 (Boynard et al., 2018).

417 The application of the OMI AKs to UKESM1.0 had the largest impacts on the simulated trends with changes
418 in a negative direction from of 0.21 (-0.37, 0.78; *p*=0.59) to -0.57 (-1.58, 0.45; *p*=0.98) DU/decade, -0.11 (-
419 0.50, 0.29; *p*=0.59) to -0.72 (-1.77, 0.32; *p*=0.16) DU/decade and -0.16 (-0.94, 0.62; *p*=0.67) to -0.62 (-
420 2.24, 1.00; *p*=0.44) DU/decade for the respective regions. IASI-FORLI AKs introduced small decreases from -
421 0.13 (-0.75, 0.49; *p*=0.67) to -0.32 (-0.82, 0.20; *p*=0.22) DU/decade, -0.28 (-0.77, 0.20; *p*=0.25) to -0.43 (-
422 1.21, 0.35; *p*=0.27) DU/decade and -0.03 (-0.62, 0.56; *p*=0.93) to -0.29 (-0.80, 0.22; *p*=0.25) DU/decade.
423 IASI-SOFRID AKs introduced small increases in the LTCO₃ trend from -0.24 (-0.85, 0.37; *p*=0.44) to -0.04 (-
424 0.53, 0.45; *p*=0.87) DU/decade, -0.27 (-0.72, 0.19; *p*=0.24) to 0.08 (-0.33, 0.49; *p*=0.69) DU/decade and -
425 0.42 (-0.97, 0.13; *p*=0.12) to -0.24 (-0.67, 0.20; *p*=0.28) DU/decade.

426 As the absolute model trends are small, it is difficult to determine the impact of the AKs on the simulated
427 trends. In relative terms, it can have impacts of several 100% but the model and model+AK trend ranges
428 (95% confidence interval) always intersect. Therefore, in an attempt to derive more substantial UKESM1.0
429 LTCO₃ trends (without and with AKs applied), to assess the maximum impact the AKs can have on UKESM

430 LTCO₃ trends, the modelled data were sorted from lowest to highest and the trend re-calculated. In North
431 America, this approach forced positive model trends, sub-sampled to OMI, IASI-FORLI and IASI-SOFRID, of
432 0.73 (0.22, 1.25; $p=0.00$), 0.64 (-3.50, 4.77; $p=0.76$) and 0.80 (0.41, 1.19; $p=0.00$) DU/decade. When the
433 AKs were applied, it yielded trends of -0.74 (-1.89, 0.40; $p=0.20$), 0.55 (0.08, 1.03; $p=0.02$) and 0.58 (0.24,
434 0.92; $p=0.00$) DU/decade. In Europe, this forced positive trends model trends, of 0.62 (0.14, 1.10; $p=0.01$),
435 0.37 (-0.05, 0.79; $p=0.08$) and 0.46 (0.09, 0.84; $p=0.01$) DU/decade, respectively. With the AKs applied, the
436 trends become 0.47 (-0.51, 1.44; $p=0.34$), 0.28 (-0.38, 0.94; $p=0.40$) and 0.10 (-0.32, 0.51; $p=0.64$)
437 DU/decade. Finally, in East Asia, the forced model trends are 0.90 (0.34, 1.47; $p=0.00$), 0.66 (0.15, 1.17; $p=$
438 0.01) and 0.63 (0.26, 1.00; $p=0.00$) DU/decade. The application of the AKs introduced model trends of 1.02
439 (-0.04, 2.09; $p=0.05$), 0.08 (-0.44, 0.61; $p=0.75$) and 0.20 (-0.20, 0.61; $p=0.31$) DU/decade.

440 Even with forced trends in the UKESM1.0 regional time-series, the trends are relatively small (i.e. typically
441 less than 1.0 DU/decade in magnitude). Therefore, the application of the AKs to the forced UKESM LTCO₃
442 time-series still yields small scale change tendencies and there is overlap in the two model trend uncertainty
443 ranges (i.e. 95% confidence level). However, in relative terms, the trend changes are larger (e.g. >100% in
444 multiple cases) and there is often a shift of the modelled LTCO₃ trend uncertainty range either intersecting
445 or no longer intersecting with zero (i.e. a shift in p-value regime from <0.05 to >0.05). Therefore, in modelled
446 and satellite datasets with more substantial trends, the impacts of the AKs, and thus the satellite vertical
447 sensitivity, on LTCO₃ trends would be much greater and potentially help pinpoint sources of differences
448 between satellite products in their TO₃ temporal evolution.

449 Section 3.3. Diurnal Variability on Regional LTCO₃ and Temporal Evolution

450 As TO₃ varies diurnally due to meteorological and photochemical processes (e.g. Gaudel et al., 2018), the
451 different satellite overpass times (i.e. Aura and MetOp-A daytime overpasses are around 13:30 and 09:30
452 local time, respectively) will likely influence the spatial distributions of TO₃ which OMI and IASI will retrieve.
453 In principle, this could therefore explain some differences between the two sensors and their long-term
454 LTCO₃ trends. The model is a useful tool to help investigate this and we used the 6-hourly output to derived
455 the UKESM simulated LTCO₃ spatial distributions at the Aura (13.30 LT) and MetOp-A (09.30 LT) day-time
456 overpasses. These model fields were then used to calculate regional time-series for North America, Europe
457 and East Asia. For each region and month, between 2008 and 2017, we calculated the regional average
458 absolute difference (i.e. from the selection of model grid cells which fell within the HTAP-2 mask for a
459 specific month) and the standard deviation of the absolute differences between the overpass times. Here,
460 across all months and regions, we found the peak average absolute difference (13:30 LT – 09:30 LT) and
461 standard deviation to be small at 2.03 and 2.56%, respectively. For the long-term trends, across all regions
462 and overpass times, all of the UKESM trends were smaller than ±0.5 DU/decade. Therefore, the model LTCO₃
463 regional trends are negligibly different between overpass times. This might not be surprising given the
464 negligible model trends in the satellite spatio-temporal trend comparisons (see Section 3.1), but the actual
465 absolute differences (average and range) in simulated LTCO₃ are also small supporting the argument that on
466 the regional scale, the day-time diurnal cycle differences between satellite overpass times has limited
467 influence on the reported satellite trend discrepancies (e.g. in Gaudel et al., 2018).

468

469 **2.4. Discussion**

470 Investigation of satellite LTCO₃ focussed on 2008 to 2017, representing a decade of overlap of the OMI and
471 IASI records. The analysis focussed on North America, Europe and East Asia as these regions are subject to
472 large emissions of and temporal changes in O₃ precursor gases. LTCO₃ is typically spatially homogeneous
473 with shallow gradients between background and source-induced O₃ concentrations. Secondly, individual
474 retrievals of LTCO₃ are often associated with large uncertainties (e.g. random and systematic uncertainties).

Formatted: Font colour: Auto

Formatted: Indent: Left: 0.63 cm, Hanging: 0.63 cm, Outline numbered + Level: 1 + Numbering Style: 1, 2, 3, ... + Start at: 1 + Alignment: Left + Aligned at: 0.63 cm + Indent at: 1.27 cm

Formatted: Font colour: Auto

475 ~~There are multiple contributory factors concerning both instrumental attributes (notably spectroradiometric~~
476 ~~noise and calibration accuracy) and variability in geophysical variables which influence radiative transfer and~~
477 ~~vertical sensitivity (e.g. stratospheric ozone, cloud and aerosol, water vapour, surface spectral~~
478 ~~reflectivity/emissivity and pressure and temperature profile) which can result in LTCO₃ time-series with~~
479 ~~substantial variability/noise when derived at high spatial resolution (e.g. when deriving time-series from data~~
480 ~~gridded at 0.5° or 1.0°). Therefore, we undertake our analysis at the regional (e.g. continental) scale where~~
481 ~~more satellite retrievals are included in time-series monthly means yielding a reduction in the random error~~
482 ~~component of the sample. Secondly, individual retrievals of LTCO₃ are subject to multiple issues (e.g.~~
483 ~~influences on radiative transfer and vertical sensitivity of stratospheric ozone, cloud and other particulates,~~
484 ~~surface spectral reflectivity/emissivity and temperature profile) which can result in noisy LTCO₃ time-series~~
485 ~~at high resolution (e.g. when gridded on a scale of 0.5° or 1.0°). Both of these factors supported analysis at a~~
486 ~~regional scale (e.g. continental scale).~~

487 Ideally, this analysis would have utilised several more records (e.g. several UV-Vis and IR products) to
488 quantify long-term trends in LTCO₃ and investigate the potential reasons for any discrepancies, as shown by
489 Gaudel et al., (2018) for TCO₃. While RAL Space, and other providers, have generated UV-Vis profile O₃
490 products for more instruments, e.g. from the Global Ozone Monitoring Experiment 1 & 2 (GOME-1 & GOME-
491 2) and the SCanning Imaging Absorption spectroMeter for Atmospheric CartograpHY (SCIAMACHY), the
492 GOME-1 and SCIAMACHY records do not overlap for as long with IASI and step changes in the GOME-2A
493 Level-1 processing scheme used to produce the available LTCO₃ Level-2 version mean it is not sufficiently
494 homogeneous (see Pope et al., (2023)). For the IR instruments, other potential sensors include the
495 Tropospheric Emissions Spectrometer (TES; Richards et al., 2008) and the RAL Space IASI Extended Infrared
496 Microwave Sounding (IMS; Pimlott et al., 2022) scheme applied to IASI. Unfortunately, the TES record only
497 covers 2005 to 2013, with decreasing spatial coverage with time, and at the time of this work the IASI-IMS
498 product had only been processed on a sub-sampled basis of 1 in 10 days.

499 In this work, we some find discrepancies in the observed long-term tendencies from the utilised LTCO₃
500 products in these northern hemispheric regions. The OMI product is subject to large-scale interannual
501 variability over the 2008-17 decade, in comparison with which the underlying linear trends are small in
502 absolute terms with large confidence ranges (i.e. 95% confidence intervals) intersecting with zero. .
503 However, the OMI LTCO₃ product has been shown to be stable over this period relative to ozonesondes by
504 Pope et al., (2023). IASI-FORLI has substantial negative LTCO₃ tendencies, but this is driven by a specific
505 discontinuity in 2010 due to inhomogeneity in Eumetsat (water vapour, temperature) data used in IASI-
506 FORLI Level-2 processing (Boynard et al., 2018; Wespes et al., 2018). It induces an artificial drift that explains
507 the substantial negative LTCO₃ trends reported here and in Gaudel et al., (2018). The IASI-SOFRID LTCO₃ and
508 apriori are very similar, with little inter-annual variability, which suggests that the IASI-SOFRID O₃ retrieval in
509 this height-range is more constrained by the apriori (~~i.e. less TO₃ sensitivity than the other products – see~~
510 ~~S3 less TO₃ sensitivity than the other products~~). Importantly, analysis of the three products' apriori LTCO₃
511 records show negligible trends meaning that year-to-year spatiotemporal sampling differences (i.e. the
512 number of retrievals used in the spatial-monthly regional averages) are not skewing long-term satellite
513 trends. In summary: any underlying linear trend in LTCO₃ occurring during the decade 2008-17 was masked
514 by interannual variability in the OMI retrieval and by constraint to the apriori in the IASI-SOFRID retrieval
515 and, although substantial for IASI-FORLI retrieval, ~~that is that is due to changing meteorological inputs to the~~
516 ~~data processing (Boynard et al., 2018; Wespes et al., 2018), believed to be due to changing meteorological~~
517 ~~input to the data processing.~~

Formatted: Font colour: Auto

Formatted: Font colour: Auto

Formatted: Font colour: Auto

518 For UKESM1.0, the model exhibits negligible temporal variability in L_{TCO}₃ for all regions and instruments’
519 samplings. Modelled L_{TCO}₃ trends never exceeded 1.0 DU/decade in magnitude, all of which were deemed
520 to be insignificant due to large associated p-values by the linear-seasonal trend model detailed in **Section 2.4**
521 **3** and **Equations 4-2 & 53**. The ozonesondes for each region were included to ground truth the model and
522 satellite trends. The North American sites’ L_{TCO}₃ time-series was relatively noisy and exhibited considerable
523 inter-annual variability in its seasonal cycle. The comparatively low level of inter-annual variability in the
524 European UKESM1.0 record of L_{TCO}₃ was in good agreement with the ozonesondes, however, and so was its
525 low trend, providing confidence in the model over that region. For East Asia, the interannual variability
526 differed substantially between UKESM1.0 and ozonesondes and the reported ozonesonde trend was
527 significantly much larger than for UKESM1.0. Therefore, when considering UKESM1.0 and the ozonesondes,
528 no consistent L_{TCO}₃ trends can be determined for any of the regions. Overall, taking all data sets into
529 account, L_{TCO}₃ appears to have neither increased nor decreased markedly over these three regions between
530 the beginning and end of the study decade (i.e. 2008 to 2017).

531 One key aspect of this work was to exploit UKESM1.0 to determine the importance of vertical sensitivity on
532 retrieved L_{TCO}₃ and how this influences the reported long-term tendency. In terms of the absolute model
533 trends (with and without the satellite AKs), the impact on L_{TCO}₃ was small with typically near-zero
534 tendencies and large uncertainty ranges (i.e. the 95% confidence interval). In relative terms, the changes in
535 model trend values were more substantial in the order of 100%. To explore this further, the UKESM1.0 L_{TCO}₃
536 time-series (with and without the satellite AKs) were sorted from lowest to highest (based on annual
537 averages) to impose the most substantial trend in the model data. When the trends were re-calculated, the
538 largest model L_{TCO}₃ trends ranged between 0.37 and 0.90 DU/decade. When the AKs were applied, the
539 L_{TCO}₃ trends ranged from -0.74 to 1.02 DU/decade. Again, in relative terms, this represents a relatively large
540 impact of the AKs on simulated L_{TCO}₃ tendencies but in absolute terms, these are small changes. Though, it
541 should be noted that many of the 95% confidence intervals for these trends either shifted to intersect with
542 zero or vice versa once the AKs were applied to the model. Gaudel et al., (2018) suggested two potential
543 reasons for the L_{TCO}₃ trend discrepancies in their study:

- 544 - Time varying instrument biases/drift.
- 545 - The impact of satellite vertical sensitivity.

546 A further two important reasons are:

- 547 - Changes over time in latitude/longitude domains sampled by satellite sensors (e.g. GOME-1 has
548 substantial issues after 2003).
- 549 - The time-period used for the trend analysis.

550 ~~As stated by Boynard et al., (2018) and Wespes et al., (2018), the IASI-FORLI-v20151001 product According~~
551 ~~to Boynard et al., (2018) and Wespes et al., (2018), the IASI-FORLI-v20151001 products~~ has an artificial
552 negative drift with time explained by a discontinuity found in the Level-2 meteorological inputs taken from
553 Eumetsat. However, in the near future, a new consistent IASI-FORLI ozone climate data record will be
554 available using homogeneous Level-1 and Level-2 Eumetsat meteorological data. Analysis of OMI L_{TCO}₃ by
555 Pope et al., 2023 showed OMI L_{TCO}₃ to be temporally stable against ozonesondes. A similar analysis (not
556 shown here) indicates IASI-SOFRID L_{TCO}₃ to also be temporally stable with near-zero drift in bias. For the
557 satellite vertical sensitivity, some of our results were unexpected. While the application of the AKs to
558 UKESM1.0 can substantially shift the simulated absolute L_{TCO}₃ values and squash/stretch the seasonal
559 amplitude, the impact on the simulation L_{TCO}₃ tendencies are small in absolute terms. In relative terms, the
560 impacts can be large (e.g. 100% change in trend rate). However, as the UKESM1.0 simulated L_{TCO}₃ trends

561 are generally near-zero, it is difficult to confidently say either way if the vertical sensitivity, when retrieving
562 LTO₃, is important for influencing long-term tendencies, even when a more substantial trend is forced upon
563 UKESM1.0. Future work on this would probably need to look at artificial model data which already has
564 substantial TO₃ trends in it (e.g. 5.0 or 10.0 DU/decade). This will obviously not match reality but would
565 provide some further quantification on how important vertical sensitivity is from different
566 instruments/sounders in LTO₃ trend determination.

567 As for year-to-year spatiotemporal sampling, our results suggest negligible trends for the product LTO₃
568 apriori time-series and thus monthly sampling biases are unlikely to be introducing artificial trends as the
569 apriori datasets are trendless. Finally, the time-period over which the trend analysis is undertaken is critically
570 important. Gaudel et al., (2018), using the available data at the time, focussed on 2005-2015/6 and 2008-
571 2015/6 for the OMI and IASI products they used. For the IASI products, using a slightly extended time-period,
572 the trends show similar tendencies. However, for OMI, 2016 and 2017 represent lower years of TO₃. As a
573 result, this dampens the strong significant positive trends reported by Gaudel et al., (2018) in TCO₃. It is
574 notable that the substantial positive increase in tropical LTO₃ between 1995 and 2017 reported by Pope et
575 al., (2023) from a series of UV-Vis sounders, included the same OMI global dataset as that is used here,
576 further suggests the selection of time period and geographical region to be crucial in regard to the role of
577 interannual variability on linear trend detection.

578 3.5. Conclusions

579 Gaudel et al., (2018) undertook a multi-satellite analysis of long-term trends in tropospheric column ozone
580 (TCO₃). They found large scale differences between these products with no clear consensus on the signs or
581 drivers of these TCO₃ trends. To avoid complications with tropopause definition and reduce influence of
582 stratospheric ozone on retrieved values, this study has undertaken a detailed follow-up assessment of
583 decadal trends in LTO₃ (surface – 450 hPa layer) rather than TCO₃ exploiting ozonesonde records, model
584 simulations and accounting carefully for satellite O₃ metrics (e.g. averaging kernels, AKs, apriori information
585 and satellite uncertainties). We have focussed on LTO₃ data sets from Ozone Monitoring Instrument (OMI)
586 produced by the RAL Space scheme and from Infrared Atmospheric Sounding Interferometer produced by
587 the IASI-FORLI and IASI-SOFRID schemes, for which there were consistent records from 2008-2017.

588 Evaluation of satellite LTO₃ from these three products over the North American, European and East Asian
589 regions resulted in linear trends which varied over a small range close to zero and with confidence intervals
590 intersecting with zero. This was consistent with simulations from the UK Earth System Model (UKESM1.0).
591 There were no large-scale trends in the apriori information, so changes in satellite year-to-year
592 spatiotemporal sampling has not been driving inconsistencies between products. When convolving
593 UKESM1.0 with the satellite AKs (i.e. to assess the impact of the satellite vertical sensitivity) it did change the
594 size of the model trend, and in some instances, the direction of the trend, but as the simulated LTO₃ trends
595 were small and insignificant, they had limited influence. Overall, our results show that changes in LTO₃
596 during the decade 2008-2017 in North America, Europe and East Asia were dominated by variability in
597 processes which control LTO₃ on shorter timescales.

598 In the near future, the new European polar orbiting mission MetOp Second Generation will include IASI Next
599 Generation and Sentinel-5 UV/VIS sounders to provide height-resolved ozone products to extend current
600 missions through to the mid-2040s. This will be supplemented by the new USA Near Earth Orbit Network
601 (NEON) series as a replacement for the Joint Polar Satellite System (JPSS). The Geostationary Environment
602 Monitoring Spectrometer (GEMS) and Tropospheric Emissions: Monitoring of Pollution (TEMPO) have also
603 recently been launched and there will be new geostationary platforms: the Infrared Sounder (IRS) and

Formatted: Indent: Left: 0.63 cm, Hanging: 0.63 cm,
Outline numbered + Level: 1 + Numbering Style: 1, 2, 3,
... + Start at: 1 + Alignment: Left + Aligned at: 0.63 cm
+ Indent at: 1.27 cm

Formatted: Font colour: Auto

604 Sentinel-4 UV/VIS sounder on Europe's Meteosat-Third Generation (MTG-S), again through to the mid-
605 2040s, and the USA Geostationary Extended Observations (GeoXO) series. Overall, these platforms will
606 provide large volumes of data (e.g. diurnal observations) and over a long-time scale on tropospheric ozone
607 for future regional trend analyses. In the future, new polar orbiting missions including the IASI Next
608 Generation and Sentinel 5 UV/VIS sounders on the MetOp Second Generation will provide tropospheric
609 ozone products to extend current missions through to the mid-2040s. There will also be the new
610 geostationary platforms like the Infrared Sounder (IRS) and Sentinel 4 UV/VIS sounder on Meteosat Third
611 Generation (MTG-S) and the already in orbit Geostationary Environment Monitoring Spectrometer (GEMS)
612 and Tropospheric Emissions: Monitoring of Pollution (TEMPO), which will provide large volumes of data (e.g.
613 diurnal observations) and over a long-time scale on tropospheric ozone for future regional trend analyses.

614 **Acknowledgements**

615 This work was funded by the UK Natural Environment Research Council (NERC) by providing funding for the
616 National Centre for Earth Observation (NCEO, award reference NE/R016518/1) and funding from the
617 European Space Agency (ESA) Climate Change Initiative (CCI) post-doctoral fellowship scheme (award
618 reference 4000137140). For UKESM1.0 model runs, we acknowledge use of the Monsoon2 system, a
619 collaborative facility supplied under the Joint Weather and Climate Research Programme, a strategic
620 partnership between the Met Office and NERC. IASI is a joint mission of EUMETSAT and the Centre National
621 d'Etudes Spatiales (CNES, France). The IASI-SOFRID research was conducted at LAERO with some financial
622 support from the CNES French spatial agency (TOSCA-IASI project). The authors acknowledge the AERIS data
623 infrastructure for providing access to the IASI-FORLI data, ULB-LATMOS for the development of the FORLI
624 retrieval algorithm, and the AC SAF project of the EUMETSAT for providing IASI-FORLI data used in this
625 paper. Anna Maria Trofaier (ESA Climate Office) provided support and advice throughout the fellowship.

626 **Data Availability**

627 The IASI-FORLI and IASI-SOFRID data can be obtained from <https://iasi.aeris-data.fr/O3> and <https://iasi-sofrid.sedoo.fr/>. The RAL OMI data is available via the NERC Centre for Environmental Data Analysis (CEDA)
628 Jasmin platform subject to data requests. However, the RAL Space satellite data, as well as the UKESM1.0
629 simulations, will be uploaded to the Zenodo open access portal (<https://zenodo.org/>) if this manuscript is
630 accepted for publication in ACP after the peer-review process. The ozonesonde data for WOUDC, SHADOZ
631 and NOAA is available from <https://woudc.org/>, <https://tropo.gsfc.nasa.gov/shadoz/> and
632 <https://gml.noaa.gov/ozwv/ozsondes/>.

634 **Author Contributions**

635 RJP conceptualised, planned and undertook the research study. BB, ELF, BJK, RS, BGL, AB and CW provided
636 the OMI and IASI ozone data and advice on using the products and their analysis. FO and MD provided
637 advice and expertise on using and running UKESM. CR provided advice and help during RP's ESA CCI
638 fellowship. Scientific and technical contributions came from MPC, WF, MAP, SSD and RR. RJP prepared the
639 manuscript with input from all co-authors. RJP conceptualised, planned and undertook the research study.
640 BB, ELF, BJK, RS, BGL, LJV, AB and CW provided the OMI and IASI ozone data and advice on using the
641 products. FO and MD provided advice and expertise on using and running UKESM. CR provided advice and
642 help during RP's ESA CCI fellowship. RJP prepared the manuscript with scientific and technical contributions
643 from all co-authors.

644 **Conflicts of Interest**

645 The authors declare no conflicts of interest.

646 **References:**

Formatted: Font colour: Auto

647 Archibald, A.T., O'Connor, F.M., Abraham, N.L., Archer-Nicholls, S., Chipperfield, M.P., Dalvi, M., Folberth,
648 G.A., Dennison, F., Dhomse, S.S., Griffiths, P.T., Hardacre, C., Hewitt, A.J., Hill, R.S., Johnson, C.E., Keeble, J.,
649 Kohler, M.O., Morgenstern, O., Mulcahy, J.P., Ordonez, C., Pope, R.J., Rumbold, S.T., Russo, M.R., Savage,
650 N.H., Sellar, A., Stringer, M., Turnock, S.T., Wild, O. and Zeng, G.: Description and evaluation of the UKCA
651 stratosphere–troposphere chemistry scheme (StratTrop v1.0) implemented in UKESM1. *Geoscientific*
652 *Model Development*, **13**, 1223–1266, doi: 10.5194/gmd-13-1223-2020, 2020.

653 Barret, B., Emili, E., Le Flochmoen, E. 2020. A tropopause-related climatological a priori profile for IASI-
654 SOFRID ozone retrievals: improvements and validation. *Atmospheric Measurement Techniques*, **13**, 5237–
655 5257, doi: 10.5194/amt-13-5237-2020.

656 Boersma, K.F., Jacob, D.J., Eskes, H.J., Pinder, R.W., Wang, J. and van der A, R.J.: Intercomparison of
657 SCIAMACHY and OMI tropospheric NO₂ columns: Observing the diurnal evolution of chemistry and emissions
658 from space. *Journal of Geophysical Research: Atmospheres*, **113 (D16S26)**, doi: 10.1029/2007JD008816,
659 2008.

660 Boersma, K. F., Eskes, H. J., Dirksen, R. J., van der A, R. J., Veefkind, J. P., Stammes, P., Huijnen, V., Kleipool,
661 Q. L., Sneep, M., Claas, J., Leitão, J., Richter, A., Zhou, Y., and Brunner, D.: An improved tropospheric
662 NO₂ column retrieval algorithm for the Ozone Monitoring Instrument, *Atmospheric Measurement*
663 *Techniques*, **4**, 1905–1928, doi: 10.5194/amt-4-1905-2011, 2011.

664 Boynard, A., Clerbaux, C., Coheur, P.-F., Hurtmans, D., Turquety, S., George, M., Hadji-Lazaro, J., Keim, C.,
665 and Meyer-Arnek, J.: Measurements of total and tropospheric ozone from IASI: comparison with correlative
666 satellite, ground-based and ozonesonde observations, *Atmos. Chem. Phys.*, **9**, 6255–6271,
667 <https://doi.org/10.5194/acp-9-6255-2009>, 2009.

668 Boynard, A., Hurtmans, D., Garane, K., Goutail, F., Hadji-Lazaro, J., Koukoulis, M. E., Wespes, C., Vigouroux, C.,
669 Keppens, A., Pommereau, J.-P., Pazmino, A., Balis, D., Loyola, D., Valks, P., Sussmann, R., Smale, D., Coheur,
670 P.-F., and Clerbaux, C.: Validation of the IASI FORLI/EUMETSAT ozone products using satellite (GOME-2),
671 ground-based (Brewer–Dobson, SAOZ, FTIR) and ozonesonde measurements, *Atmospheric Measurement*
672 *Techniques*, **11**, 5125–5152, <https://doi.org/10.5194/amt-11-5125-2018>, 2018.

673 Chang, K. L., Cooper, O. R., Gaudel, A., Petropavlovskikh, I., & Thouret, V.: Statistical regularization for trend
674 detection: an integrated approach for detecting long-term trends from sparse tropospheric ozone profiles.
675 *Atmospheric Chemistry and Physics*, **20(16)**, 9915–9938, 2020.

676 Clerbaux, C., Boynard, A., Clarisse, L., George, M., Hadji-Lazaro, J., Herbin, H., Hurtmans, D., Pommier, M.,
677 Razavi, A., Turquety, S., Wespes, C. and Coheur, P.F.: Monitoring of atmospheric composition using the
678 thermal infrared IASI/MetOp sounder, *Atmospheric Chemistry and Physics*, **9 (16)**, 6041–6054,
679 doi:10.5194/acp-9-6041-2009, 2009.

680 Doherty, R. M., Heal, M. R., and O'Connor, F. M.: Climate change impacts on human health over Europe
681 through its effect on air quality, *Environmental Health*, **16(1)**, 33–44, doi:10.1186/s12940-017-0325-2, 2017.

682 ESA. 2019. Climate Change Initiative. <http://cci.esa.int/ozone> (last accessed 01/09/2022).

683 Eskes HJ and Boersma KF. 2003. Averaging kernels for DOAS total column satellite retrievals. *Atmospheric*
684 *Chemistry and Physics*, **3**, 1285–1291, doi: 10.5194/acp-3-1285-2003.

685 European Commission, Joint Research Centre, Dentener F, et al. 2016. Hemispheric Transport of Air Pollution
686 (HTAP): specification of the HTAP2 experiments: ensuring harmonized modelling, Publications Office,
687 <https://data.europa.eu/doi/10.2788/725244>.

Formatted: Line spacing: single

Formatted: Font:

Formatted: Font colour: Auto

688 Eyring, V., Bony, S., Meehl, G. A., Senior, C. A., Stevens, B., Stouffer, R. J., and Taylor, K. E.: Overview of the
689 Coupled Model Intercomparison Project Phase 6 (CMIP6) experimental design and organization, *Geosci.*
690 *Model Dev.*, 9, 1937–1958, <https://doi.org/10.5194/gmd-9-1937-2016>, 2016. Gaudel A, et al. 2018.
691 Tropospheric Ozone Assessment Report: Present day distribution and trends of tropospheric ozone relevant
692 to climate and global atmospheric chemistry model evaluation. *Elementa*, 6 (39), 1-58, doi:
693 10.1525/elementa.291.

694 [Fiore, Arlene M., et al. \(2022\), Understanding recent tropospheric ozone trends in the context of large](#)
695 [internal variability: A new perspective from chemistry-climate model ensembles, *Environmental Research:*](#)
696 [Climate, *https://doi.org/10.1088/2752-5295/ac9cc2.*](#)

697 Forster, P., Storelvmo, T., Armour, K., Collins, W., Dufresne, J.-L., Frame, D., Lunt, D. J., Mauritsen, T.,
698 Palmer, M. D., Watanabe, M., Wild, M., and Zhang, H.: The Earth's Energy Budget, Climate Feedbacks, and
699 Climate Sensitivity, in: *Climate Change 2021: The Physical Science Basis, Contribution of Working Group I to*
700 *the Sixth Assessment Report of the Intergovernmental Panel on Climate Change*, edited by: Masson-
701 Delmotte, V., Zhai, P., Pirani, A., Connors, S. L., Péan, C., Berger, S., Caud, N., Chen, Y., Goldfarb, L., Gomis, M.
702 I., Huang, M., Leitzell, K., Lonnoy, E., Matthews, J. B. R., Maycock, T. K., Waterfield, T., Yelekçi, O., Yu, R., and
703 Zhou, B., Cambridge University Press, Cambridge, United Kingdom and New York, NY, USA, 923–1054,
704 doi:10.1017/9781009157896.009, 2021.

705 Gaudel, A., Cooper, O.R., Ancellet, G., Barret, B., Boynard, A., Burrows, J.P., Clerbaux, C., Coheur, P.F.,
706 Cuesta, J., Cuevas, E., Doniki, S., Dufour, G., Ebojje, F., Foret, G., Garia, O., Granados-Munoz, M.J., Hannigan,
707 J.W., Hase, F., Hassler, B., Huang, G., Hurtmans, D., Jaffe, D., Jones, N., Kalabokas, P., Kerridge, B., Kulwaik, S.,
708 Latter, B., Leblanc, T., Le Flochmoen, E., Lin, W., Liu, J., Liu, X., Mahieu, E., McClure-Begley, A., Neu, J.L.,
709 Osman, M., Palm, M., Petetin, H., Petropavlovskikh, I., Querel, R., Rahpoe, N., Rozanov, A., Schultz, M.G.,
710 Schwab, J., Siddans, R., Smale, D., Steinbacher, M., Tanimoto, H., Tarasick, D.W., Thouret, V., Thompson,
711 A.M., Trickl, T., Weatherhead, E., Wespes, C., Worden, H.M., Vigouroux, C., Xu, X., Zeng, G. and Ziemke, J.:
712 Tropospheric Ozone Assessment Report: Present day distribution and trends of tropospheric ozone relevant
713 to climate and global atmospheric chemistry model evaluation. *Elementa*, 6(39), 1-58,
714 doi:10.1525/elementa.291, 2018.

715 Gauss, M., Myhre, G., Isaksen, I. S. A., Grewe, V., Pitari, G., Wild, O., Collins, W. J., Dentener, F. J., Ellingsen,
716 K., Gohar, L. K., Hauglustaine, D. A., Iachetti, D., Lamarque, F., Mancini, E., Mickley, L. J., Prather, M. J., Pyle,
717 J. A., Sanderson, M. G., Shine, K. P., Stevenson, D. S., Sudo, K., Szopa, S., and Zeng, G.: Radiative forcing since
718 preindustrial times due to ozone change in the troposphere and the lower stratosphere, *Atmospheric*
719 *Chemistry and Physics*, 6, 575–599, <https://doi.org/10.5194/acp-6-575-2006>, 2006.

720 Hoesly, R. M., Smith, S. J., Feng, L., Klimont, Z., Janssens-Maenhout, G., Pitkanen, T., Seibert, J. J., Vu, L.,
721 Andres, R. J., Bolt, R. M., Bond, T. C., Dawidowski, L., Kholod, N., Kurokawa, J.-I., Li, M., Liu, L., Lu, Z., Moura,
722 M. C. P., O'Rourke, P. R., and Zhang, Q.: Historical (1750–2014) anthropogenic emissions of reactive gases
723 and aerosols from the Community Emissions Data System (CEDS), *Geoscientific Model Development*, 11,
724 369–408, <https://doi.org/10.5194/gmd-11-369-2018>, 2018.

725 Hollaway, M.J., Arnold, S.R., Challinor, A. J. and Emberson, L.D: Intercontinental trans-boundary
726 contributions to ozone-induced crop yield losses in the North Hemisphere, *Biogeosciences*, 9, 271–2929, doi:
727 10.5194/bg-9-271-2012, 2012.

728 [Hubert, D., Lambert, J.-C., Verhoelst, T., Granville, J., Keppens, A., Baray, J.-L., Bourassa, A.E., Cortesi, U.,](#)
729 [Degenstein, D.A., Froidevaux, L., Godin-Beekmann, S., Hoppel, K.W., Johnson, B.L., Kyrola, E., Leblanc, T.,](#)
730 [Lichtenberg, G., Marchand, M., McElroy, C.T., Murtagh, D., Nakane, H., Portafaix, T., Querel, R., Russell, J.M.,](#)

Formatted: Font colour: Auto

731 [Salvador, J., Smit, H.G.J., Stebel, K., Steinbrecht, W., Strawbridge, K.B., Stubi, R., Swart, D.P.J., Taha, G.,](#)
732 [Tarasick, D.W., Thompson, A.M., Urban, J., van Gijsel, J.A.E., Van Malderen, R., von der Gathen P., Walker,](#)
733 [K.A., Wolfram, E. and Zawodny, J.M.: Ground-based assessment of the bias and long-term stability of 14 limb](#)
734 [and occultation ozone profile data records. *Atmospheric Measurement Techniques*, 9, 2497-2534, doi:](#)
735 [10.5194/amt-9-2497-2016, 2016.](#)

736 Illingworth, S. M., Remedios, J. J., Boesch, H., Moore, D. P., Sembhi, H., Dudhia, A., and Walker, J. C.: ULIRS,
737 an optimal estimation retrieval scheme for carbon monoxide using IASI spectral radiances: sensitivity
738 analysis, error budget and simulations, *Atmospheric Measurements Techniques*, 4, 269–288, doi:
739 10.5194/amt-4-269-2011, 2011.

740 Keim, C., Eremenko, M., Orphal, J., Dufour, G., Flaud, J.-M., Höpfner, M., Boynard, A., Clerbaux, C., Payan, S.,
741 Coheur, P.-F., Hurtmans, D., Claude, H., Dier, H., Johnson, B., Kelder, H., Kivi, R., Koide, T., López Bartolomé,
742 M., Lambkin, K., Moore, D., Schmidlin, F. J., and Stübi, R.: Tropospheric ozone from IASI: comparison of
743 different inversion algorithms and validation with ozone sondes in the northern middle latitudes,
744 *Atmospheric Chemistry and Physics*, 9, 9329–9347, doi: 10.5194/acp-9-9329-2009, 2009.

745 [Keppens, A., Lambert, J.-C., Graille, J., Hubert, D., Verhoelst, T., Compennolle, S., Latter, B., Kerridge, B.,](#)
746 [Siddans, R., Boynard, A., Hadji-Lazaro, J., Clerbaux, C., Wespes, C., Hurtmans, D.R., Coheur, P.-F., van Peet,](#)
747 [J.C.A., van der A, R.J., Garane, K., Koukouli, M.E., Balis, D.S., Delcloo, A., Kivi, R., Stubi, R., Godin-Beekmann,](#)
748 [S., Van Roozendael, M. and Zehner, C.: Quality assessment of the Ozone_cci Climate Research Data Package](#)
749 [\(release 2017\) – Part 2: Ground-based validation of nadir ozone profile data products. *Atmospheric*](#)
750 [Measurement Techniques](#), 11, 3769-3800, doi: 10.5194/amt-11-3769-2018, 2018.

751 [Keppens, A., Compennolle, S., Verhoelst, T., Hubert, D., and Lambert, J.-C.: Harmonization and comparison of](#)
752 [vertically resolved atmospheric state observations: methods, effects, and uncertainty budget, *Atmos. Meas.*](#)
753 [Tech.](#), 12, 4379–4391, <https://doi.org/10.5194/amt-12-4379-2019>, 2019.

754 ▲

755 Lamarque, J.-F., Bond, T. C., Eyring, V., Granier, C., Heil, A., Klimont, Z., Lee, D., Liousse, C., Mieville, A.,
756 Owen, B., Schultz, M. G., Shindell, D., Smith, S. J., Stehfest, E., Van Aardenne, J., Cooper, O. R., Kainuma, M.,
757 Mahowald, N., McConnell, J. R., Naik, V., Riahi, K., and van Vuuren, D. P.: Historical (1850–2000) gridded
758 anthropogenic and biomass burning emissions of reactive gases and aerosols: methodology and application,
759 *Atmospheric Chemistry and Physics*, 10, 7017–7039, doi: 10.5194/acp-10-7017-2010, 2010.

760 Matthes, K., Funke, B., Andersson, M. E., Barnard, L., Beer, J., Charbonneau, P., Clilverd, M. A., Dudok de Wit,
761 T., Haberer, M., Hendry, A., Jackman, C. H., Kretschmar, M., Kruschke, T., Kunze, M., Langematz, U.,
762 Marsh, D. R., Maycock, A. C., Misios, S., Rodger, C. J., Scaife, A. A., Seppälä, A., Shangguan, M., Sinnhuber,
763 M., Tourpali, K., Usoskin, I., van de Kamp, M., Verronen, P. T., and Versick, S.: Solar forcing for CMIP6 (v3.2),
764 *Geoscientific Model Development*, 10, 2247–2302, <https://doi.org/10.5194/gmd-10-2247-2017>, 2017.

765 McPeters, R.D., Labow, G.J., and Logan, J.A. 2007. Ozone climatological profiles for satellite retrieval
766 algorithms. *Journal of Geophysical Research*, 112 (D05308), <https://doi.org/10.1029/2005JD006823>.

767 Miles, G.M., Siddans, R., Kerridge, B. J., Latter, B. G., and Richards, N. A. D.: Tropospheric ozone and ozone
768 profiles retrieved from GOME-2 and their validation, *Atmospheric Measurement Techniques*, 8, 385–398,
769 doi:10.5194/amt-8-385-2015, 2015.

770 Monks, S.A., Arnold, S.R., Hollaway, M. J., Pope, R.J., Wilson, C., Feng, W., Emmerson, K.E., Kerridge, B.J.,
771 Latter, B.L., Miles, G.M., Siddans, R. and Chipperfield, M.P.: The TOMCAT global chemistry transport model
772 v1.6: Description of chemical mechanism and model evaluation, *Geoscientific Model Development*, 10 (8),
773 3025–3057, doi:10.5194/gmd-10-3025-2017, 2017.

Formatted: Font colour: Auto

Formatted: Font: +Body (Calibri), 11 pt, Font colour: Auto

Formatted: Default, Line spacing: single, Adjust space between Latin and Asian text, Adjust space between Asian text and numbers

774 Myhre, G., Shindell, D., Bréon, F.-M, Collins, W., Fuglestvedt, J., Huang, J., Koch, D., Lamarque, J.-F., Lee, D.,
775 Mendoza, B., Nakajima, T., Robock, A., Stephens, G., Takemura, T. and Zhang, H.: Anthropogenic and Natural
776 Radiative Forcing, in: Climate Change 2013: The Physical Science Basis. Contribution of Working Group I to
777 the Fifth Assessment Report of the Intergovernmental Panel on Climate Change, Cambridge University Press,
778 Cambridge, United Kingdom and New York, NY, USA, 659–740, 2013.

779 O'Connor, F. M., Johnson, C. E., Morgenstern, O., Abraham, N. L., Braesicke, P., Dalvi, M., Folberth, G. A.,
780 Sanderson, M. G., Telford, P. J., Voulgarakis, A., Young, P. J., Zeng, G., Collins, W. J., and Pyle, J. A.: Evaluation
781 of the new UKCA climate-composition model – Part 2: The Troposphere, *Geoscientific Model Development*,
782 7, 41–91, doi: 10.5194/gmd-7-41-2014, 2014.

783 Pimlott, M.A., Pope, R.P., Kerridge, B.J., Latter, B.G., Knappett, D.S., Heard, D.E., Ventress, L.J., Siddans, R.,
784 Feng, W. and Chipperfield, M.P.: Investigating the global OH radical distribution using steady-state
785 approximations and satellite data. *Atmospheric Chemistry and Physics*, **22**, 10467-10488, doi: 10.5194/acp-
786 22-10467-2022, 2022.

787 Pope, R.J., Arnold, S.R., Chipperfield, M.P., Latter, B.G., Siddans, R. and Kerridge, B.J.: Widespread changes in
788 UK air quality observed from space. *Atmospheric Science Letters*, **19:e817**, doi: 10.1002/asl.817.

789 Pope, R. J., Kerridge, B. J., Siddans, R., Latter, B. G., Chipperfield, M. P., Feng, W., Pimlott, M. A., Dhomse, S.
790 S., Retscher, C., and Rigby, R.: Investigation of spatial and temporal variability in lower tropospheric ozone
791 from RAL Space UV–Vis satellite products, *Atmospheric Chemistry and Physics*, **23**, 14933–14947,
792 <https://doi.org/10.5194/acp-23-14933-2023>, 2023.

793 [Pope, R. J., Rap, A., Pimlott, M. A., Barret, B., Le Flochmoen, E., Kerridge, B. J., Siddans, R., Latter, B. G.,
794 Ventress, L. J., Boynard, A., Retscher, C., Feng, W., Rigby, R., Dhomse, S. S., Wespes, C. and Chipperfield, M.
795 P.: Quantifying the tropospheric ozone radiative effect and its temporal evolution in the satellite era,
796 *Atmospheric Chemistry and Physics*, **24**, 3613-3626, doi: 10.5194/acp-24-3613-2024, 2024.](#)

797 Rao, S., Klimont, Z., Smith, S.J., Van Dingenen, R., Dentener, F., Bouwman, L., Riahi, K., Amann, M., Bodirsky,
798 B.L., van Vuuren, D.P., Reus, L.R., Calvin, K., Drouet, L., Fricko, O., Fujimori, S., Gernaat, D., Havlik, P.,
799 Harmsen, M., Hasegawa, T., Heyes, C. and Tavoni, M.: Future air pollution in the shared socio-economic
800 pathways. *Global Environmental Change*, **42**, 346-358, doi: 10.1016/j.gloenvcha.2016.05.012.

801 Richards, N.A.D, Osterman, G.B., Browell, E.V., Hair, J.W., Avery, M. and Li, Q.: Validation of tropospheric
802 emission spectrometer ozone profiles with aircraft observations during the intercontinental chemical
803 transport experiment–B. *Journal Geophysical Research*, **113**(D16S29), doi: 10.1029/2007JD008815, 2008.

804 [Russo, M. R., Kerridge, B. J., Abraham, N. L., Keeble, J., Latter, B. G., Siddans, R., Weber, J., Griffiths, P. T.,
805 Pyle, J. A., and Archibald, A. T.: Seasonal, interannual and decadal variability of tropospheric ozone in the
806 North Atlantic: comparison of UM-UKCA and remote sensing observations for 2005–2018, *Atmos. Chem.
807 Phys.*, **23**, 6169–6196, <https://doi.org/10.5194/acp-23-6169-2023>, 2023.](#)

808 Sellar, A.A., Jones, C.G., Mulcahy, J.P., Tang, Y., Yool, A., Wiltshire, A., O'Connor, F.M., Stringer, M., Hill, R.,
809 Palmieri, J., Woodward, S., de Mora, L., Kuhlbrodt, T., Rumbold, S.T., Kelley, D.I., Ellis, R., John, C.E., Walton,
810 J., Abraham, N.L., Andrews, M.B., Andrews, T., Archibald, A.T., Berthou, S., Burke, E., Blockley, E., Carslaw, K.,
811 Dalvi, M., Edwards, J., Folbert, G.A., Gedney, N., Griffiths, P.T., Harper, A.B., Hendry, M.A., Hewitt, A.J.,
812 Johnson, B., Jones, A., Jones, C.D., Keebie, J., Liddicoat, S., Morgenstern, O., Parker, R.J., Predoi, V.,
813 Robertson, E., Siahann, A., Smith, R.S., Swaminathan, R., Woodhouse, M.T., Zeng, G. and Zerroukat, M.:
814 Description and Evaluation of the UK Earth System Model. *Journal of Advances in Modeling Earth Systems*,
815 **11**, 4513-4558, doi: 10.1029/2019MS001739, 2019.

Formatted: Font colour: Auto

Formatted: Line spacing: single

816 Sindelarova, K., Granier, C., Bouarar, I., Guenther, A., Tilmes, S., Stavrakou, T., Müller, J.-F., Kuhn, U., Stefani,
817 P., and Knorr, W.: Global data set of biogenic VOC emissions calculated by the MEGAN model over the last
818 30 years, *Atmos. Chem. Phys.*, **14**, 9317–9341, doi: 10.5194/acp-14-9317-2014, 2014.

819 Sitch, S., Cox, P.M., Collins, W.J., & Huntingford, C.: Indirect radiative forcing of climate change through
820 ozone effects on the land carbon sink, *Nature*, **448**, 791–795, doi:10.1038/nature06059, 2007.

821 [Sofieva, V. F., Tamminen, J., Kyrölä, E., Mielonen, T., Veefkind, P., Hassler, B., and Bodeker, G. E.: A novel
822 tropopause-related climatology of ozone profiles, *Atmos. Chem. Phys.*, **14**, 283–
823 299, <https://doi.org/10.5194/acp-14-283-2014>, 2014.](https://doi.org/10.5194/acp-14-283-2014)

824 Telford, P. J., Braesicke, P., Morgenstern, O., and Pyle, J. A.: Technical Note: Description and assessment of a
825 nudged version of the new dynamics Unified Model, *Atmospheric Chemistry and Physics*, **8**, 1701–1712,
826 <https://doi.org/10.5194/acp-8-1701-2008>, 2008.

827 van der A, R.J., Peters, D.H.M.U., Eskes, H., Boersma, K.F., Van Roozendaal, M., De Smedt, I. and Kelder,
828 H.M.: Detection of the trend and seasonal variation in tropospheric NO₂ over China. *Journal of Geophysical
829 Research*, **11**, D12317, doi: 10.1029/2005JD006594, 2006.

830 van der A, R.J., Eskes, H.J., Boersma, K.F., van Noije, T.P.C., Van Roozendaal, M., De Smedt, I., Peters,
831 D.H.M.U. and Meijer, E.W.: Trends, seasonal variability and dominant NO_x sources derived from a ten year
832 record of NO₂ measured from space. *Journal of Geophysical Research*, **113**, 1–12, doi:
833 10.1029/2007JD009021, 2008.

834 van der Werf, G. R., Randerson, J. T., Giglio, L., van Leeuwen, T. T., Chen, Y., Rogers, B. M., Mu, M., van
835 Marle, M. J. E., Morton, D. C., Collatz, G. J., Yokelson, R. J., and Kasibhatla, P. S.: Global fire emissions
836 estimates during 1997–2016, *Earth System Science Data*, **9**, 697–720, [https://doi.org/10.5194/essd-9-697-
837 2017](https://doi.org/10.5194/essd-9-697-2017), 2017.

838 van Marle, M. J. E., Kloster, S., Magi, B. I., Marlon, J. R., Daniiau, A.-L., Field, R. D., Arneeth, A., Forrest, M.,
839 Hantson, S., Kehrwalid, N. M., Knorr, W., Lasslop, G., Li, F., Mangeon, S., Yue, C., Kaiser, J. W., and van der
840 Werf, G. R.: Historic global biomass burning emissions for CMIP6 (BB4CMIP) based on merging satellite
841 observations with proxies and fire models (1750–2015), *Geoscientific Model Development*, **10**, 3329–3357,
842 <https://doi.org/10.5194/gmd-10-3329-2017>, 2017.

843 Weatherhead, E.C., Reinsel, G.C., Tiao, G.C., Meng, X., Choi, D., Cheang, W., Keller, T., De Luisi, J., Wuebbles,
844 D.J., Kerr, J.B., Miller, A.J., Oltmans, S.J. and Frederick, J.E.: Factors affecting the detection of trends:
845 statistical considerations and applications to environmental data. *Journal of Geophysical Research*, **103(D14)**,
846 17149–17161, doi: 10.1029/98JD00995, 1998.

847 Wespes, C., Hurtmans, D., Clerbaux, C., Boynard, A., and Coheur, P.-F. 2018. Decrease in tropospheric O₃
848 levels in the Northern Hemisphere observed by IASI. *Atmospheric Chemistry and Physics*, **18**, 6867–6885,
849 doi:10.5194/acp-18-6867-2018.

850 WHO (World Health Organisation), Ambient (outdoor) air pollution, available at: [https://www.who.int/news-
851 room/fact-sheets/detail/ambient-\(outdoor\)-air-quality-and-health](https://www.who.int/news-room/fact-sheets/detail/ambient-(outdoor)-air-quality-and-health) (last accessed 2nd January 2024), 2022.

852 Wiltshire, A.J., Burke, E.J., Chadburn, S.E., Jones, C.D., Cox, P.M., Davies-Barnard, T., Friedlingstein, P.,
853 Harper, A.B., Liddicoat, S., Sitch, S. and Zaehle, S.: JULES-CN: a coupled terrestrial carbon–nitrogen scheme
854 (JULES vn5.1). *Geophysical Model Development*, **14** (4), 2161–2186, doi: 10.5194/gmd-14-2161-2021,
855 2021. Yool A, et al. 2013. MEDUSA-2.0: an intermediate complexity biogeochemical model of the marine

Formatted: Font colour: Auto

Formatted: Font colour: Auto

Formatted: Font colour: Auto

Formatted: Font colour: Auto

Formatted: Font colour: Auto

Formatted: Font colour: Auto

856 carbon cycle for climate change and ocean acidification studies. *Geoscientific Model Development*, **6**, 1767–
 857 1811, doi: 10.5194/gmd-6-1767-2013.

858 [WMO, Meteorology – A three-dimensional science, World Meteorological Organisation, Bulletin 6, \(Oct\),](#)
 859 [134–138, 1957,](#)

860 Young, P.J., Archibald, A.T., Bowman, K.W., Lamarque, J-F., Naik, V., Stevenson, D.S., Tilmes, S., Voulgarakis,
 861 A., Wild, O., Bergmann, D., Cameron-Smith, P., Cionni, I., Collins, W.J., Dalsoren, S.B., Doherty, R.M., Eyring,
 862 V., Faluvegi, G., Horowitz, L.W., Josse, B., Lee, Y.H., MacKenzie, I.A., Nagashima, T., Plummer, D.A., Righi, M.,
 863 Rumbold, S.T., Skeie, R.B., Shindell, D.T., Strode, S.A., Sudo, K., Szopa, S. and Zeng. G.: Pre-industrial to end
 864 21st century projections of tropospheric ozone from the Atmospheric Chemistry and Climate Model
 865 Intercomparison Project (ACCMIP). *Atmospheric Chemistry and Physics*, **13**, 2063-2090, doi: 10.5194/acp-13-
 866 2063-2013, 2013.

867 Ziemke, J.R., Chandra, S., Labow, G.J., Bhartia, P.K., Froidevaux, L. and Witte, J.C.: A global climatology of
 868 tropospheric and stratospheric ozone derived from Aura OMI/MLS measurements, *Atmospheric Chemistry*
 869 *and Physics*, **11**, 9237-9251, doi: /10.5194/acp-11-9237-2011, 2011.

870

871

872

873

874 **Figures & Tables:**

875

Data Provider	Satellite Profile Products & Version	Product Link	Data Range	Data Size
RAL Space	OMI-fv214	http://www.ceda.ac.uk/	2004-2018	1442 GB
ATMOS-ULB	IAS-FORLI-v20151001	https://iasi.aeris-data.fr/catalog/	2008-2019	9.1 TB
Université de Toulouse	IASI-SOFRID vn3.5	https://iasi-sofrid.sedoo.fr/	2008-2017	3.0 TB

876

877 **Table 1:** List of the satellite ozone profile data sets.

878

Satellite	Quantity	Trend	Trend Lower	Trend Upper	p-value	Fit (R ²)
OMI	Trend	-0.79	-7.07	5.48	0.80	0.58
	Trend Error 1	-1.50	-7.04	4.04	0.59	0.68
	Trend Error 2	-0.09	-6.98	6.81	0.98	0.50
	Apriori Trend	-0.05	-0.21	0.11	0.56	1.00
	UKESM Trend	0.21	-0.37	0.78	0.47	0.95
	UKESM+AKs Trend	-0.57	-1.58	0.45	0.26	0.90
	UKESM Trend Forced	0.73	0.22	1.25	0.00	0.95
UKESM+AKs Trend Forced	-0.74	-1.89	0.40	0.20	0.89	
FORLI	Trend	-1.42	-2.25	-0.50	0.00	0.93
	Trend Error 1	-1.34	-2.21	-0.47	0.00	0.93
	Trend Error 2	-1.50	-2.51	-0.50	0.00	0.93

Formatted: Font colour: Auto

Formatted: Font colour: Auto

Formatted: Font colour: Auto

Formatted Table

	Apriori-Trend	0.00	-0.11	0.12	0.94	0.67
	UKESM-Trend	-0.13	-0.75	0.49	0.67	0.93
	UKESM+AKs-Trend	-0.32	-0.83	0.20	0.22	0.92
	UKESM-Trend-Forced	0.64	-3.50	4.77	0.76	0.46
	UKESM+AKs-Trend-Forced	0.55	0.08	1.03	0.02	0.93
SOFRIID	Trend	0.12	-0.59	0.82	0.74	0.94
	Trend-Error-1	0.14	-0.59	0.88	0.70	0.90
	Trend-Error-2	0.09	-0.48	0.66	0.75	0.94
	Apriori-Trend	0.11	-0.17	0.29	0.43	0.98
	UKESM-Trend	-0.24	-0.85	0.37	0.44	0.95
	UKESM+AKs-Trend	-0.04	-0.53	0.45	0.87	0.97
	UKESM-Trend-Forced	0.80	0.41	1.19	0.00	0.97
	UKESM+AKs-Trend-Forced	0.58	0.24	0.92	0.00	0.98
OMI	Trend	-0.80	-7.29	5.69	0.80	0.71
	Trend-Error-1	-1.65	-6.92	3.62	0.53	0.76
	Trend-Error-2	0.05	-7.44	7.53	0.99	0.67
	Apriori-Trend	-0.12	-0.26	0.03	0.10	1.00
	UKESM-Trend	-0.11	-0.50	0.29	0.59	0.99
	UKESM+AKs-Trend	-0.72	-1.77	0.22	0.16	0.95
	UKESM-Trend-Forced	0.62	0.14	1.10	0.01	0.98
	UKESM+AKs-Trend-Forced	0.47	-0.51	1.44	0.24	0.94
FORLI	Trend	-1.83	-2.78	-0.89	0.00	0.92
	Trend-Error-1	-1.90	-2.72	-0.88	0.00	0.93
	Trend-Error-2	-1.87	-2.87	-0.87	0.00	0.92
	Apriori-Trend	0.09	-0.09	0.27	0.32	0.48
	UKESM-Trend	-0.28	-0.77	0.20	0.25	0.98
	UKESM+AKs-Trend	-0.43	-1.21	0.35	0.27	0.94
	UKESM-Trend-Forced	0.37	-0.05	0.79	0.08	0.98
	UKESM+AKs-Trend-Forced	0.28	-0.38	0.94	0.40	0.93
SOFRIID	Trend	0.05	-0.91	1.01	0.92	0.93
	Trend-Error-1	0.16	-0.74	1.07	0.72	0.91
	Trend-Error-2	-0.07	-0.91	0.78	0.87	0.93
	Apriori-Trend	0.17	-0.12	0.45	0.24	0.98
	UKESM-Trend	-0.27	-0.72	0.19	0.24	0.98
	UKESM+AKs-Trend	0.08	-0.33	0.49	0.69	0.98
	UKESM-Trend-Forced	0.46	0.09	0.84	0.01	0.99
	UKESM+AKs-Trend-Forced	0.10	-0.22	0.51	0.64	0.98
OMI	Trend	-0.09	-7.88	7.70	0.98	0.51
	Trend-Error-1	-1.05	-6.61	4.52	0.70	0.66
	Trend-Error-2	0.87	-8.24	9.98	0.85	0.38
	Apriori-Trend	-0.25	-0.71	0.22	0.29	0.98
	UKESM-Trend	-0.16	-0.94	0.62	0.67	0.98
	UKESM+AKs-Trend	-0.62	-2.24	1.00	0.44	0.95
	UKESM-Trend-Forced	0.90	0.34	1.47	0.00	0.99

	UKESM+AKs Trend Forced	1.02	-0.04	2.09	0.05	0.97
FORLI	Trend	-1.52	-2.16	-0.88	0.00	0.93
	Trend Error 1	-1.42	-2.06	-0.78	0.00	0.93
	Trend Error 2	-1.62	-2.27	-0.98	0.00	0.92
	Apriori Trend	-0.03	-0.22	0.16	0.76	0.21
	UKESM Trend	-0.03	-0.62	0.56	0.93	0.98
	UKESM+AKs Trend	-0.29	-0.80	0.22	0.25	0.95
	UKESM Trend Forced	0.66	0.15	1.17	0.01	0.98
	UKESM+AKs Trend Forced	0.08	-0.44	0.61	0.75	0.92
SOFRIID	Trend	-0.19	-1.01	0.62	0.65	0.96
	Trend Error 1	-0.08	-0.72	0.58	0.82	0.90
	Trend Error 2	-0.30	-1.02	0.42	0.41	0.93
	Apriori Trend	-0.15	-0.39	0.09	0.21	0.98
	UKESM Trend	-0.42	-0.97	0.13	0.12	0.99
	UKESM+AKs Trend	-0.24	-0.67	0.20	0.28	0.98
	UKESM Trend Forced	0.63	0.26	1.00	0.00	0.99
	UKESM+AKs Trend Forced	0.29	-0.20	0.61	0.31	0.98

Table 2: LTCO₂ trends (DU/decade) for the satellite trend (Trend), the satellite uncertainty trend (Trend Error 1), the satellite+uncertainty trend (Trend Error 2), the satellite apriori trend (Apriori Trend), UKESM trend (UKESM Trend), UKESM with AKs applied trend (UKESM+AKs Trend), UKESM forced trend (UKESM Trend Forced) and UKESM with AKs applied forced trend (UKESM+AKs Trend Forced). The trends from OMI, IASI-FORLI and IASI-SOFRIID are for North America (red), Europe (blue) and East Asia (green). The trend lower and trend upper represent the trend 95% confidence interval. R² is the trend fit skill (i.e. correlation squared) and the p value is also shown.

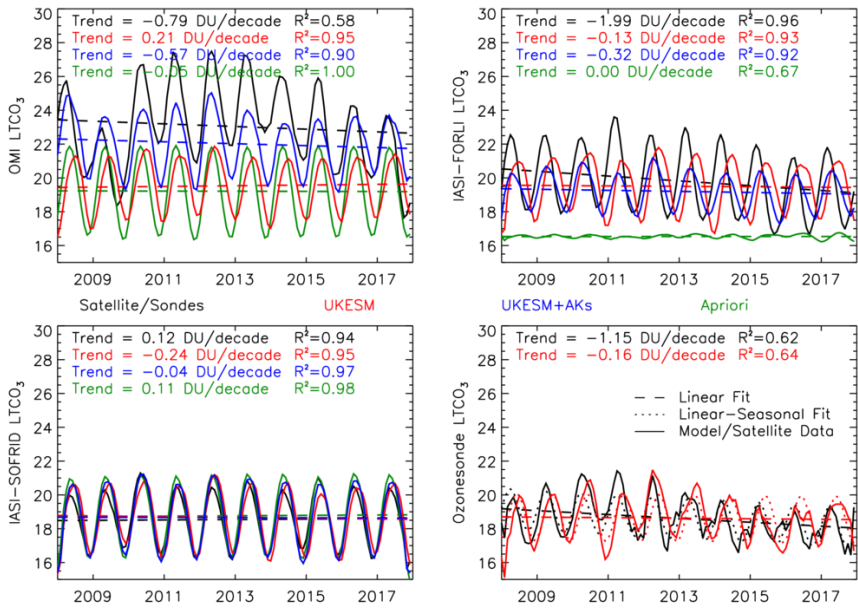
Satellite	Quantity	Trend	Trend Lower	Trend Upper	p-value	Fit (R ²)
OMI – North America	Trend	-0.79	-7.07	5.48	0.80	0.58
	Trend Error 1	-1.50	-7.04	4.04	0.59	0.68
	Trend Error 2	-0.09	-6.98	6.81	0.98	0.50
	Apriori Trend	-0.05	-0.21	0.11	0.56	1.00
	UKESM Trend	0.21	-0.37	0.78	0.47	0.95
	UKESM+AKs Trend	-0.57	-1.58	0.45	0.26	0.90
	UKESM Trend Forced	0.73	0.22	1.25	0.00	0.95
	UKESM+AKs Trend Forced	-0.74	-1.89	0.40	0.20	0.89
FORLI – North America	Trend	-1.42	-2.35	-0.50	0.00	0.93
	Trend Error 1	-1.34	-2.21	-0.47	0.00	0.93
	Trend Error 2	-1.50	-2.51	-0.50	0.00	0.93
	Apriori Trend	0.00	-0.11	0.12	0.94	0.67
	UKESM Trend	-0.13	-0.75	0.49	0.67	0.93
	UKESM+AKs Trend	-0.32	-0.83	0.20	0.22	0.92
	UKESM Trend Forced	0.64	-3.50	4.77	0.76	0.46

	<u>UKESM+AKs Trend Forced</u>	<u>0.55</u>	<u>0.08</u>	<u>1.03</u>	<u>0.02</u>	<u>0.93</u>
SOFRID – North America	<u>Trend</u>	<u>0.12</u>	<u>-0.59</u>	<u>0.82</u>	<u>0.74</u>	<u>0.94</u>
	<u>Trend Error 1</u>	<u>0.14</u>	<u>-0.59</u>	<u>0.88</u>	<u>0.70</u>	<u>0.90</u>
	<u>Trend Error 2</u>	<u>0.09</u>	<u>-0.48</u>	<u>0.66</u>	<u>0.75</u>	<u>0.94</u>
	<u>Apriori Trend</u>	<u>0.11</u>	<u>-0.17</u>	<u>0.39</u>	<u>0.43</u>	<u>0.98</u>
	<u>UKESM Trend</u>	<u>-0.24</u>	<u>-0.85</u>	<u>0.37</u>	<u>0.44</u>	<u>0.95</u>
	<u>UKESM+AKs Trend</u>	<u>-0.04</u>	<u>-0.53</u>	<u>0.45</u>	<u>0.87</u>	<u>0.97</u>
	<u>UKESM Trend Forced</u>	<u>0.80</u>	<u>0.41</u>	<u>1.19</u>	<u>0.00</u>	<u>0.97</u>
	<u>UKESM+AKs Trend Forced</u>	<u>0.58</u>	<u>0.24</u>	<u>0.92</u>	<u>0.00</u>	<u>0.98</u>
OMI -Europe	<u>Trend</u>	<u>-0.80</u>	<u>-7.29</u>	<u>5.69</u>	<u>0.80</u>	<u>0.71</u>
	<u>Trend Error 1</u>	<u>-1.65</u>	<u>-6.92</u>	<u>3.62</u>	<u>0.53</u>	<u>0.76</u>
	<u>Trend Error 2</u>	<u>0.05</u>	<u>-7.44</u>	<u>7.53</u>	<u>0.99</u>	<u>0.67</u>
	<u>Apriori Trend</u>	<u>-0.12</u>	<u>-0.26</u>	<u>0.03</u>	<u>0.10</u>	<u>1.00</u>
	<u>UKESM Trend</u>	<u>-0.11</u>	<u>-0.50</u>	<u>0.29</u>	<u>0.59</u>	<u>0.99</u>
	<u>UKESM+AKs Trend</u>	<u>-0.72</u>	<u>-1.77</u>	<u>0.32</u>	<u>0.16</u>	<u>0.95</u>
	<u>UKESM Trend Forced</u>	<u>0.62</u>	<u>0.14</u>	<u>1.10</u>	<u>0.01</u>	<u>0.98</u>
	<u>UKESM+AKs Trend Forced</u>	<u>0.47</u>	<u>-0.51</u>	<u>1.44</u>	<u>0.34</u>	<u>0.94</u>
FORLI - Europe	<u>Trend</u>	<u>-1.83</u>	<u>-2.78</u>	<u>-0.89</u>	<u>0.00</u>	<u>0.92</u>
	<u>Trend Error 1</u>	<u>-1.80</u>	<u>-2.72</u>	<u>-0.88</u>	<u>0.00</u>	<u>0.93</u>
	<u>Trend Error 2</u>	<u>-1.87</u>	<u>-2.87</u>	<u>-0.87</u>	<u>0.00</u>	<u>0.92</u>
	<u>Apriori Trend</u>	<u>0.09</u>	<u>-0.09</u>	<u>0.27</u>	<u>0.32</u>	<u>0.48</u>
	<u>UKESM Trend</u>	<u>-0.28</u>	<u>-0.77</u>	<u>0.20</u>	<u>0.25</u>	<u>0.98</u>
	<u>UKESM+AKs Trend</u>	<u>-0.43</u>	<u>-1.21</u>	<u>0.35</u>	<u>0.27</u>	<u>0.94</u>
	<u>UKESM Trend Forced</u>	<u>0.37</u>	<u>-0.05</u>	<u>0.79</u>	<u>0.08</u>	<u>0.98</u>
	<u>UKESM+AKs Trend Forced</u>	<u>0.28</u>	<u>-0.38</u>	<u>0.94</u>	<u>0.40</u>	<u>0.93</u>
SOFRID – Europe	<u>Trend</u>	<u>0.05</u>	<u>-0.91</u>	<u>1.01</u>	<u>0.92</u>	<u>0.93</u>
	<u>Trend Error 1</u>	<u>0.16</u>	<u>-0.74</u>	<u>1.07</u>	<u>0.72</u>	<u>0.91</u>
	<u>Trend Error 2</u>	<u>-0.07</u>	<u>-0.91</u>	<u>0.78</u>	<u>0.87</u>	<u>0.93</u>
	<u>Apriori Trend</u>	<u>0.17</u>	<u>-0.12</u>	<u>0.45</u>	<u>0.24</u>	<u>0.98</u>
	<u>UKESM Trend</u>	<u>-0.27</u>	<u>-0.72</u>	<u>0.19</u>	<u>0.24</u>	<u>0.98</u>
	<u>UKESM+AKs Trend</u>	<u>0.08</u>	<u>-0.33</u>	<u>0.49</u>	<u>0.69</u>	<u>0.98</u>
	<u>UKESM Trend Forced</u>	<u>0.46</u>	<u>0.09</u>	<u>0.84</u>	<u>0.01</u>	<u>0.99</u>
	<u>UKESM+AKs Trend Forced</u>	<u>0.10</u>	<u>-0.32</u>	<u>0.51</u>	<u>0.64</u>	<u>0.98</u>
OMI – East Asia	<u>Trend</u>	<u>-0.09</u>	<u>-7.88</u>	<u>7.70</u>	<u>0.98</u>	<u>0.51</u>
	<u>Trend Error 1</u>	<u>-1.05</u>	<u>-6.61</u>	<u>4.52</u>	<u>0.70</u>	<u>0.66</u>
	<u>Trend Error 2</u>	<u>0.87</u>	<u>-8.24</u>	<u>9.98</u>	<u>0.85</u>	<u>0.38</u>
	<u>Apriori Trend</u>	<u>-0.25</u>	<u>-0.71</u>	<u>0.22</u>	<u>0.29</u>	<u>0.98</u>
	<u>UKESM Trend</u>	<u>-0.16</u>	<u>-0.94</u>	<u>0.62</u>	<u>0.67</u>	<u>0.98</u>

	<u>UKESM+AKs Trend</u>	<u>-0.62</u>	<u>-2.24</u>	<u>1.00</u>	<u>0.44</u>	<u>0.95</u>
	<u>UKESM Trend Forced</u>	<u>0.90</u>	<u>0.34</u>	<u>1.47</u>	<u>0.00</u>	<u>0.99</u>
	<u>UKESM+AKs Trend Forced</u>	<u>1.02</u>	<u>-0.04</u>	<u>2.09</u>	<u>0.05</u>	<u>0.97</u>
<u>FORLI - East Asia</u>	<u>Trend</u>	<u>-1.52</u>	<u>-2.16</u>	<u>-0.88</u>	<u>0.00</u>	<u>0.93</u>
	<u>Trend Error 1</u>	<u>-1.42</u>	<u>-2.06</u>	<u>-0.78</u>	<u>0.00</u>	<u>0.93</u>
	<u>Trend Error 2</u>	<u>-1.62</u>	<u>-2.27</u>	<u>-0.98</u>	<u>0.00</u>	<u>0.92</u>
	<u>Apriori Trend</u>	<u>-0.03</u>	<u>-0.22</u>	<u>0.16</u>	<u>0.76</u>	<u>0.21</u>
	<u>UKESM Trend</u>	<u>-0.03</u>	<u>-0.62</u>	<u>0.56</u>	<u>0.93</u>	<u>0.98</u>
	<u>UKESM+AKs Trend</u>	<u>-0.29</u>	<u>-0.80</u>	<u>0.22</u>	<u>0.25</u>	<u>0.95</u>
	<u>UKESM Trend Forced</u>	<u>0.66</u>	<u>0.15</u>	<u>1.17</u>	<u>0.01</u>	<u>0.98</u>
	<u>UKESM+AKs Trend Forced</u>	<u>0.08</u>	<u>-0.44</u>	<u>0.61</u>	<u>0.75</u>	<u>0.93</u>
<u>SOFRID - East Asia</u>	<u>Trend</u>	<u>-0.19</u>	<u>-1.01</u>	<u>0.63</u>	<u>0.65</u>	<u>0.96</u>
	<u>Trend Error 1</u>	<u>-0.08</u>	<u>-0.73</u>	<u>0.58</u>	<u>0.82</u>	<u>0.90</u>
	<u>Trend Error 2</u>	<u>-0.30</u>	<u>-1.02</u>	<u>0.42</u>	<u>0.41</u>	<u>0.93</u>
	<u>Apriori Trend</u>	<u>-0.15</u>	<u>-0.39</u>	<u>0.09</u>	<u>0.21</u>	<u>0.98</u>
	<u>UKESM Trend</u>	<u>-0.42</u>	<u>-0.97</u>	<u>0.13</u>	<u>0.12</u>	<u>0.99</u>
	<u>UKESM+AKs Trend</u>	<u>-0.24</u>	<u>-0.67</u>	<u>0.20</u>	<u>0.28</u>	<u>0.98</u>
	<u>UKESM Trend Forced</u>	<u>0.63</u>	<u>0.26</u>	<u>1.00</u>	<u>0.00</u>	<u>0.99</u>
	<u>UKESM+AKs Trend Forced</u>	<u>0.20</u>	<u>-0.20</u>	<u>0.61</u>	<u>0.31</u>	<u>0.98</u>

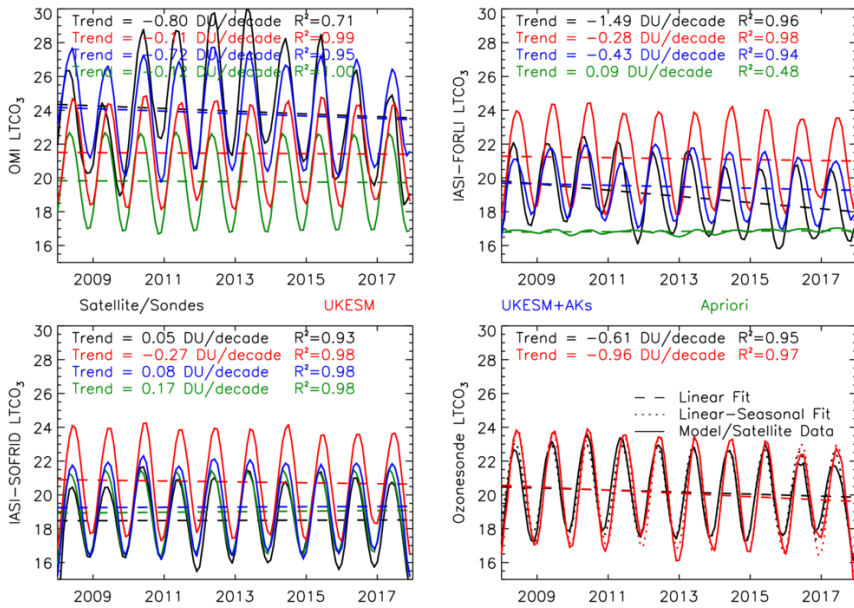
Table 2: *LTCO₂ trends (DU/decade) for the satellite trend (Trend), the satellite-uncertainty trend (Trend Error 1), the satellite+uncertainty trend (Trend Error 2), the satellite apriori trend (Apriori Trend), UKESM trend (UKESM Trend), UKESM with AKs applied trend (UKESM+AKs Trend), UKESM forced trend (UKESM Trend Forced) and UKESM with AKs applied forced trend (UKESM+AKs Trend Forced). The “trend lower” and “trend upper” represent the trend 95% confidence interval based on the trend precision calculated from Equation 3. R² is the trend fit skill (i.e. correlation squared) and the p-value is also shown.*

Formatted: Font colour: Auto



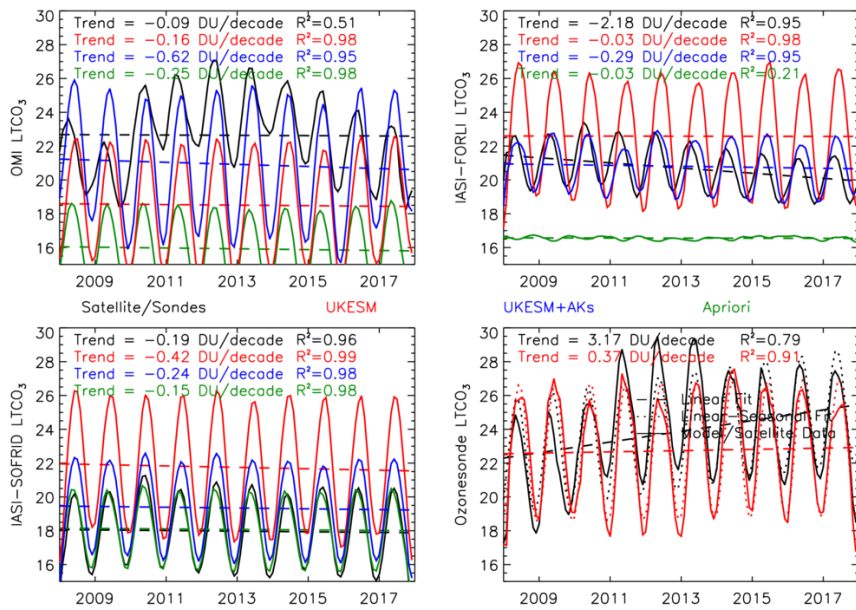
896
 897 **Figure 1:** Lower tropospheric column ozone ($LTCO_3$, surface to 450 hPa, DU) regional time-series for North
 898 America, based on the HTAP land mask, from OMI (top-left), IASI-FORLI (top-right), IASI-SOFRID (bottom-left)
 899 and ozonesondes (bottom-right) are shown by the black lines in the respective panels. UKESM simulations
 900 without and with satellite averaging kernels (AKs) applied are shown in red and blue lines. Green lines show
 901 the satellite apriori. Dashed lines show the $LTCO_3$ linear trend which are labelled in the top of each panel. The
 902 R^2 squared values show the linear-seasonal trend model fit to the corresponding $LTCO_3$ time-series (i.e.
 903 correlation squared).

904
 905



906

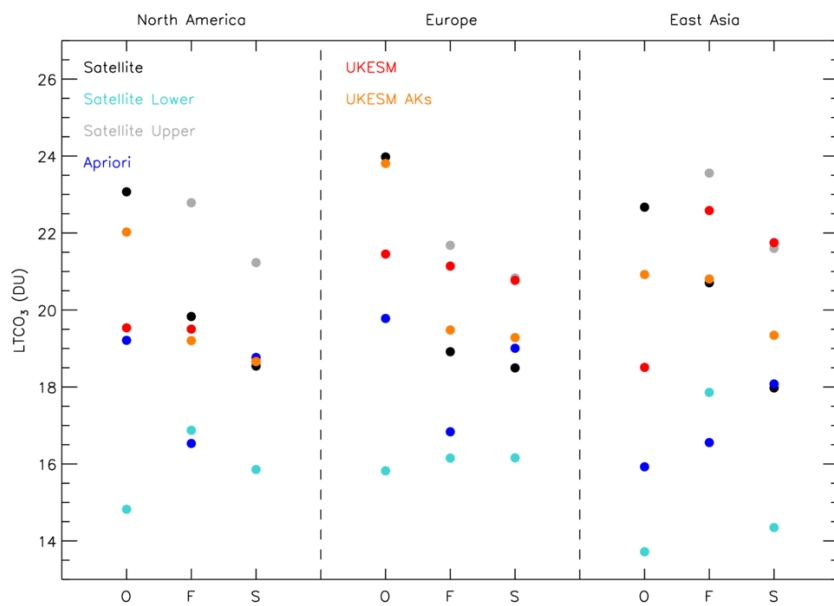
907 **Figure 2:** LTCO₃ (DU) regional time-series for Europe, based on the HTAP land mask, from OMI (top-left), IASI-
 908 FORLI (top-right), IASI-SOFRID (bottom-left) and ozonesondes (bottom-right) are shown by the black lines in
 909 the respective panels.. UKESM simulations without and with satellite AKs applied are shown in red and blue
 910 lines. Green lines show the satellite apriori. Dashed lines show the LTCO₃ linear trend which are labelled in the
 911 top of each. The R² squared values show the linear-seasonal trend model fit to the corresponding LTCO₃ time-
 912 series (i.e. correlation squared).



913

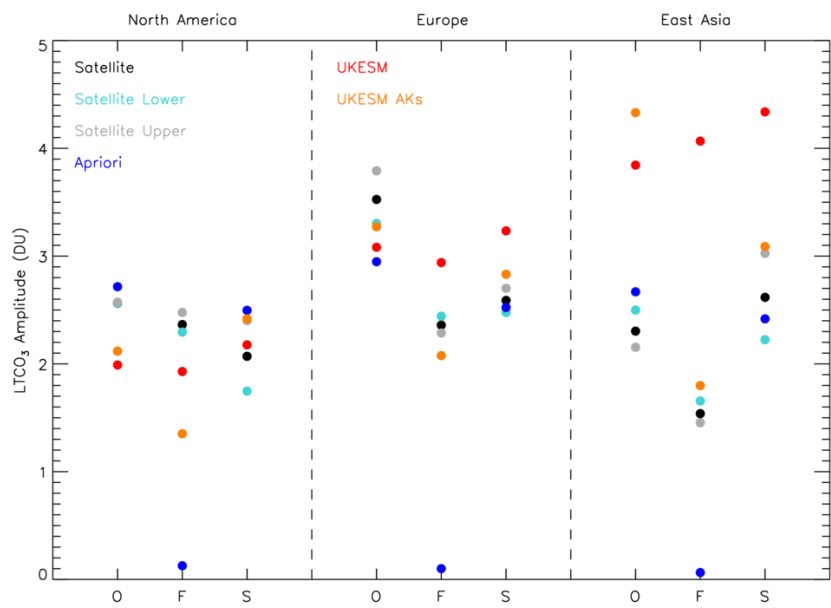
914 **Figure 3:** $LTCO_3$ (DU) regional time-series for East Asia, based on the HTAP land mask, from OMI (top-left),
 915 IASI-FORLI (top-right), IASI-SOFRID (bottom-left) and ozonesondes (bottom-right) are shown by the black lines
 916 in the respective panels.. UKESM simulations without and with satellite AKs applied are shown in red and blue
 917 lines. Green lines show the satellite apriori. Dashed lines show the $LTCO_3$ linear trend which are labelled in the
 918 top of each panel. The R^2 squared values show the linear-seasonal trend model fit to the corresponding $LTCO_3$
 919 time-series (i.e. correlation squared).

920



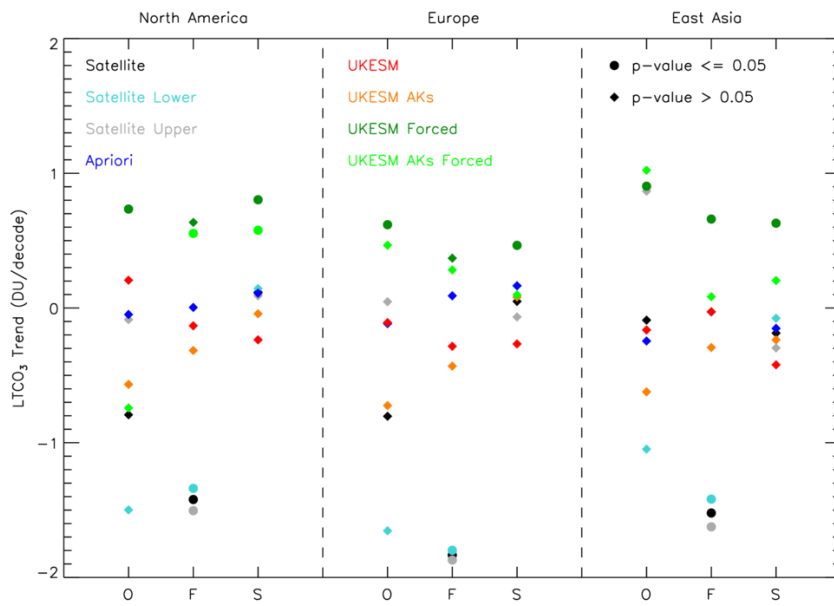
921

922 **Figure 4:** Average $LT\text{CO}_3$ (DU) values across the 2008-2017 time-period for the satellite (black), satellite-lower
 923 (cyan), satellite-upper (grey), apriori (blue), UKESM (red) and UKESM+AKs (orange). The satellite-lower and
 924 satellite-upper values are the average of the satellite \pm its error term time-series (note: these values do not
 925 always fit in the y-axis range). O, F and S represent OMI, IASI-FORLI and IASI-SOFRID for North America (left),
 926 Europe (centre) and East Asia (right).



927

928 **Figure 5:** Average $LT\text{CO}_3$ seasonal cycle amplitude (DU) values across the 2008-2017 time-period for the
 929 satellite (black), satellite-lower (cyan), satellite-upper (grey), apriori (blue), UKESM (red) and UKESM+AKs
 930 (orange). The satellite-lower and satellite-upper values are the average of the satellite \pm its error term time-
 931 series (note: these values do not always fit in the y-axis range). O, F and S represent OMI, IASI-FORLI and IASI-
 932 SOFRID for North America (left), Europe (centre) and East Asia (right).



933

934 **Figure 6:** Average $LTCO_3$ linear trends (DU/decade) values across the 2008-2017 time-period for the satellite
 935 (black), satellite-lower (cyan), satellite-upper (grey), apriori (blue), UKESM (red), UKESM+AKs (orange),
 936 UKESM forced (dark green) and UKESM+AKs forced (light green). The satellite-lower and satellite-upper
 937 values are the average of the satellite \pm its error term time-series (note: these values do not always fit in the
 938 y-axis range). O, F and S represent OMI, IASI-FORLI and IASI-SOFRID for North America (left), Europe (centre)
 939 and East Asia (right). Triangle and circular symbols represent linear trends with p-values > 0.05 or $p \leq 0.05$,
 940 respectively.

941

942

943

944